2020

Mechanical Properties of Boron Carbide (B4C)

Ruslan Kuliiev
University of Central Florida

MECHANICAL PROPERTIES OF BORON CARBIDE (B_4C)

by

RUSLAN KULIIEV
B.S. National Aviation University, Kyiv, Ukraine, 2015
M.S. National Aviation University, Kyiv, Ukraine, 2017

A thesis submitted in partial fulfillment of the requirements
for the degree of Master of Science in Aerospace Engineering
in the Department of Mechanical and Aerospace Engineering
in the College of Engineering and Computer science
at the University of Central Florida
Orlando, Florida

Spring Term
2020

Major Professor: Nina Orlovskaya

ABSTRACT

Boron carbide (B_4C) is one of the most important opaque boride ceramics that has high hardness and Young's modulus that along with low density lead to a significant resistance to ballistic impact and, thus, B_4C is broadly used as a protective material. B_4C has also high neutron capturing cross section; therefore, it is used as control rods and neutron absorption shielding in nuclear reactors. In this work thermal, electrical and mechanical properties of dense B_4C ceramics (99%) sintered using Spark Plasma Sintering (SPS) were investigated. The Young's modulus of B_4C measured by three different techniques – IE, RUS, and nanoindentation showed a very good overlap in values, which ranges from 419.2 ± 47.3 GPa for nanoindentation to 458.7 GPa for RUS measurements at room temperature. The mean contact pressure-contact depth plots obtained from load-displacement nanoindentation data indicated pop-in events during loading and an "elbow" event during unloading, both of which are indicative of possible structural changes in B_4C structure during nanoindentation. The appearance of "elbow" deviations in load-displacement nanoindentation curves of B_4C was detected for the first time. The 4-point bending strength of the B_4C ceramics was equal to 585±70 MPa with Weibull parameter of 9.9 and scale parameter equal to 611 MPa. The biaxial strength of B_4C was measured to be much lower and equal to 238.6±122 MPa with Weibull parameters of 2.2 and scale parameter equal to 271 MPa. To the best of our knowledge the biaxial strength of B_4C was also measured for the first time. In this work it was determined that failure of B_4C occurred by fully transgranular fracture, with no intergranular failure present on fracture surface. B_4C's fracture toughness $K_{Ic} = 3 \pm 0.19\ MPa \times m^{1/2}$ was measured using SEVNB technique, which is similar to previously reported values.

ACKNOWLEDGMENTS

I would like to thank to *Dr. Nina Orlovskaya* for a support and guidance throughout the MS program. Dr. Nina was able to help me, a new graduate international student from Ukraine supported by Fulbright Program, without precise knowledge about the US educational system as well as with a different cultural background to adapt to a new system and produce great results. Dr. Nina's strong research experience and cultural background obtained because of work in different countries such as the USA, Switzerland, Germany, Norway, Austria, the UK, Ukraine helped me to have a much better focus on the research development and obtain solid goals for the future.

I also would like to show my appreciation to great people and my amazing team members: *Dr. Alejandro Carrasco-Pena, Mahmud Omer, Ryan Jordan, Dexter Smith, Alina Aftab* and *Spencer Robbins* for continuous support and camaraderie. In addition, I would also like to mention a great help provided by our colleagues *Dr. Pradeep Vallachira Warriam Sasikumar, Dr. Laura Conti, Dr. Gurdial Blugan, Prof. Thomas Graule* at Empa, Swiss Federal Laboratories for Material Science and Technology, Switzerland for help with measurements of four-point bending, K_{1c} experiments as well as measurements of thermal expansion, electrical resistivity and Young's modulus by Impulse Excitation technique. A special thanks to *Dr. Yuanli Bai* and *Shutao Song* from the Department of Mechanical and Aerospace Engineering at Uiversity of Central Florida, for providing the license for Abaqus software and an amazing willingness to help at any time. I would also like to extend my thanks to *Dr. Elinor G. Castle* and *Prof. Michael John Reece* from School of Engineering and Materials Science, Queen Mary University of London, the UK for help

with Spark Plasma Sintering of B_4C samples. In addition, help with nanoindentation experiments by *Mr. Holden Hyer* and *Prof. Yongho Sohn* at the Department of Material Science and Engineering, University of Central Florida as well as the measurements of elastic properties of B_4C by Resonance Ultrasound Spectroscopy performed at Texas A & T University, College Station, TX by *Mr. DongGi Ha* and *Prof. Miladin Radovic* are greatly appreciated.

Among all, I would like to thank my family for their constant support and love! I feel very lucky to have come this far, but I wouldn't have done it without my family and friends, the ones I knew and the ones I made here, who made my stay at UCF memorable.

The work was supported in part by National Science Foundation MRI project "133778".

TABLE OF CONTENTS

LIST OF FIGURES

LIST OF TABLES

LIST OF EQUATIONS

CHAPTER 1: INTRODUCTION

Borides – A Unique Class of Ceramic Materials

Borides are very important large group of compounds that provides a wide range of useful thermal, electrical, physical and mechanical properties for a variety of engineering applications [1], [2], [3], [4]. Borides are ceramic materials which form bonds, mostly covalent bonding between boron and many other chemical elements. As boron, the chemical element #5 in periodic table, has 3 valence electrons, it tends to form strong covalent bonding in form of clustering, in which B_{12} icosahedra or cuboctahedra are common structural units [5], [6], [7], [8]. Within B - clusters, the valence electron density is high, so the covalent bonding is responsible for high melting point, high hardness, low compressibility, and low coefficient of thermal expansion. The binary compounds with boron include monoborides (TiB, MnB, CrB), diborides (MgB_2, TiB_2, HfB_2, ZrB_2), tetraborides (FeB_4, WB_4, CrB_4) and higher borides having one, two, four as well as more boron atoms in the crystal lattice of compounds, respectively.

Borides such as magnesium diboride (MgB_2), titanium diboride (TiB_2), hafnium diboride (HfB_2), zirconium diboride (ZrB_2), boron carbide (B_4C) and many others are attracting significant interest due to the demand for high-performance materials nowadays. As an example of the unique properties of borides, MgB_2 was reported to be a high temperature superconductor with a transition temperature of 39 K [9], which allowed this boride to be used in numerous exciting applications, such as Magnetic Resonance Imaging systems, fault current limiters, transformers, motors and generators, refrigerators, superconducting magnetic energy storage and magnetic levitated trains [10], [11], [12]. Another important binary boride is TiB_2, which has high hardness and wear

properties, and, thus, broadly used for example, in cutting tools inserts or electrodes in metal smelting [13], [14], among many other applications [15], [16], [17]

Some other borides, HfB_2 and ZrB_2, stand out and have a great asset for aerospace industry, mainly because of their superior thermal conductivity, oxidation resistance and high melting temperatures of over 3000˚C, which allow them to be used in critical applications of hypersonic vehicles, such as leading edges and nose cones. The photograph of the ZrB_2-SiC ceramic sample is shown in Figure 1, before and during the high temperature oxidation testing [18].

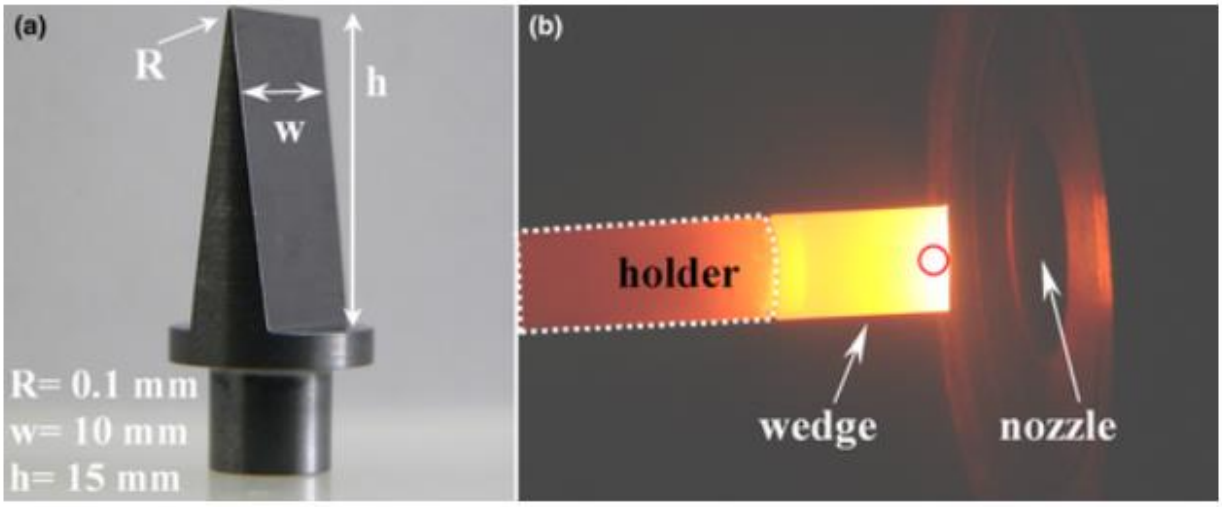

Figure 1 ZrB_2-SiC ceramic composite sample before testing (a), inside the arc-jet camera during high temperature testing (b) [18]

B_4C in another important boride ceramics. Due to its high hardness and Young's modulus, as well as very low density B_4C found an immense application as protective materials. It is used as personal body armor as well as ballistic plates for helicopters or automotive vehicles [19], [20].

Boron carbide is also broadly used as abrasives, such as sand nozzles blasters and other wear applications [21], [20], [19].

Boron carbide is being studied as a prospective material for nuclear applications as a shielding material and neutron absorbent for control rods (Figure 2) [22], [23].

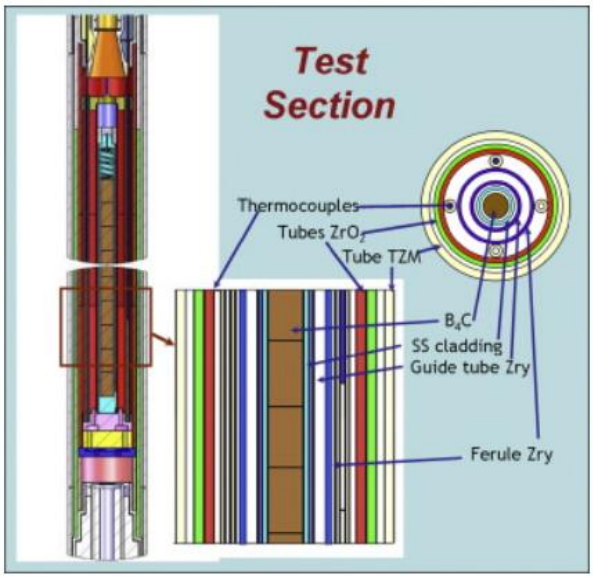

Figure 2 Scematic of B_4C control rod oxidation behaviour testing at BECARRE-III facility [24]

Excellent thermal conductivity as well as thermal shock resistance of boron carbide integrated with other compounds to form composites is suitable for nuclear fusion reactors applications [23], [25]. A schematic presentation of a bundle assembly with 21 rods is shown in Figure 3, when the central rod is a control rod with B_4C pellets surrounded by 20 rods with ZrO_2 pellets and the assembly is used in pressurized water nuclear reactors and boiling water nuclear reactors.

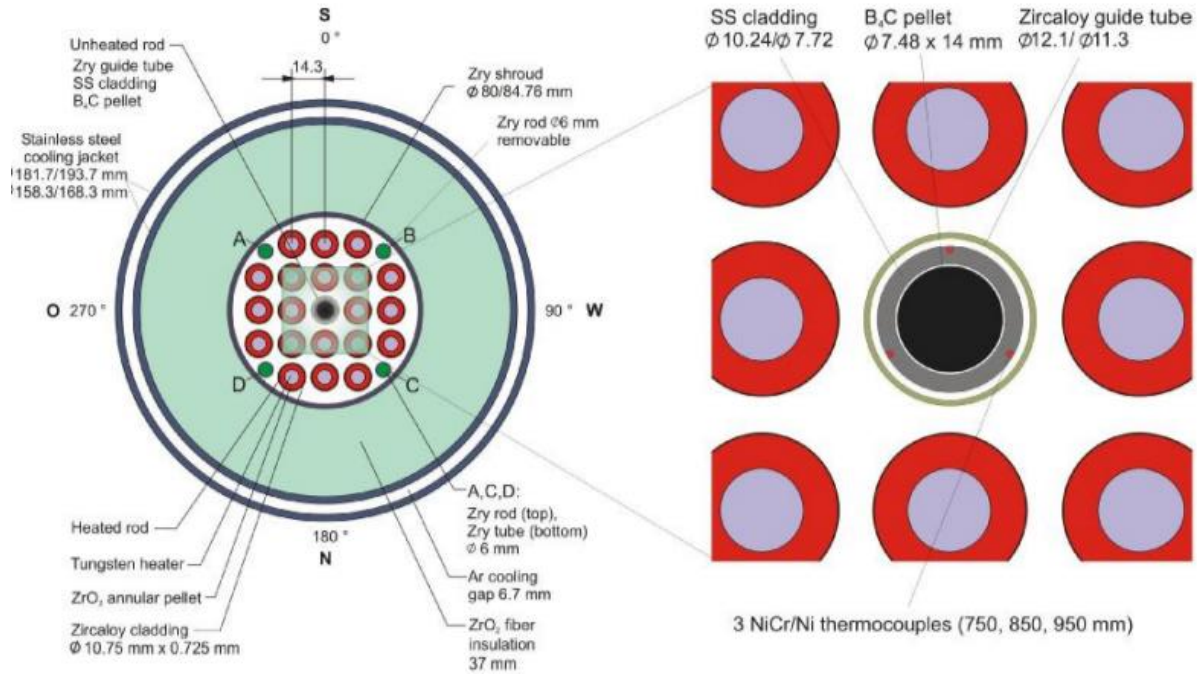

Figure 3 Schematic presentation of B_4C rods in a bundle of a QUENCH facility for control rod behavior testing [26]

Special QUENCH tests are performed to determine the degradation of B_4C control rod [26]. Neutron absorption of B_4C is also used as a therapy for cancer treatment [27]. In addition, boron carbide is a great material for electronics which operate a high temperature due to its excellent thermal properties.

Processing of Boride Ceramics

There are numerous processing techniques used to process different binary boride ceramics [9], [28], [29]. For the processing of bulk polycrystalline borides, the most used sintering techniques are pressureless sintering in the control protective atmosphere, hot pressing, hot isostatic pressing and Spark Plasma Sintering (SPS). The most recent and very promising sintering technique is a

Flash Spark Plasma Sintering (FSPS), where densification of hard to sinter borides can occure within seconds at high sintering temperatures. Below is a brief overview of sintering techniques used to process dense boride ceramics, such as B_4C, HfB_2 and ZrB_2.

Pressureless sintering

Pressureless sintering process is one of the technologically simplest ways of ceramic material production [30], [31]. In well-developed pressureless sintering technique, the powder of specific boride composition is compacted to a specific shape either using uniaxial compaction, slip casting, 3D printing to prepare the raw shape of the parts for sintering. The choice for powder compacting is mostly based on the shape complexity of the fabricated ceramics. The uniaxial die pressing is the most widely used technique of the ceramic's compaction process, which consists of two punches to which the pressure is being applied. The powder with an addition of binder to reduce friction is being places in the die between the two punches. Once the powder is placed in the die weather static or dynamic compaction is being used for the process, by applying constant pressure for typically a few seconds or a pulse pressure wave for a few milliseconds, respectively [32]. After the powder is compacted, it is placed in the furnace, typically under protective Ar environment or vacuum, for pressureless sintering. The sintering profile is chosen in the manner that it would allow to achieve a full densification of the material upon sintering at high temperature. While the sintering time could be very long, such long as 10-24 hours or more, however this technique allows to obtain parts with complex shapes that often do not need any further treatment, such as machining or sand blasting, and are ready to be used in specific applications [33], [30]. However, the sintering time for the material production is relatively high which increases the cost of energy and in addition, it is also difficult to achieve full density of the borides.

Hot pressing

Hot pressing technique of ceramics is similar to the pressureless sintering; however, the pressure is applied during high temperature sintering that significantly facilitate densification [34], [35]. Hot pressing technique allows to reduce the sintering time by applying pressure externally which allows to densify the ceramics faster [36]. The uniaxial hot pressing is usually performed in a graphite die, however, other materials, such as silicon carbide (SiC) can also be used for the packing purposes in hot pressing. After boride ceramics packing the die is placed inside of the vacuum chamber, where both high temperature and high uniaxial pressure are applied. Both induction and resistance heating can be used depending on the design of the hot press machine [36]. A schematic presentation of a graphite die packed with a powder inside ready for hot pressing is shown in the Figure 4.

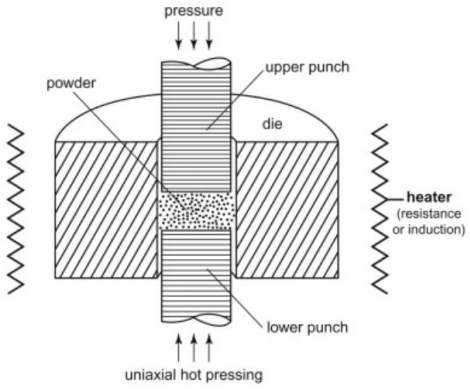

Figure 4 Hot pressing technique [36]

Hot Isostatic Pressing

Hot isostatic pressing (HIP) is very similar sintering technique to hot pressing, however, instead of uniaxial pressure used in hot pressing, the hydrostatic pressure using gas or liquid media are

applied during sintering of boride ceramics [37], [38]. It has many advantages, as the pressure values are not limited by a strength of graphite die used in hot pressing, and pressure could reach much higher values, thus, allowing to produce ceramics with better properties. Also, the shapes of the ceramics could be much more complex by using HIP, unlike the shapes of the material processed by hot pressing, when only simple shapes can be produced. The schematic setup of hot isostatic pressing is presented in Figure 5.

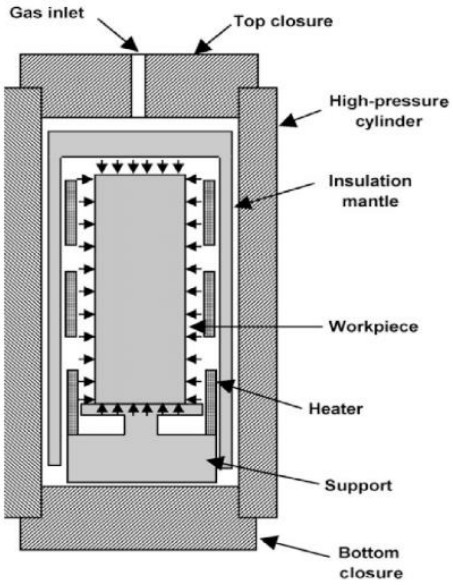

Figure 5 A schematic of hot isostatic pressing setup [39]

Spark Plasma Sintering (SPS)

Spark Plasma Sintering (SPS) technique, sometimes also called Field Assisted Sintering Technique (FAST) is used as a fast and at the same time energy efficient way of ceramics processing [40]. SPS, like hot pressing, is based on the simultaneous application of high temperature and high axial pressure, however, unlike hot pressing, the electric current also passes

through a powder specimen. Many research was performed to understand as to why the densification of the ceramics by SPS is much faster in comparison with hot pressing [41], [42]. It was specified the sintering mechanisms during SPS includes the diffusion, electromigration, surface tension, as well as effect of external load that all contribute to the fast sintering, which typically occurs both at lower temperatures and shorten time as compared to the hot pressing. The high heating rates also increase the sinterability of the powder by suppressing surface diffusion at the early stages of sintering, in addition to promoting limited grain growth of ceramics [41], [43]. In [41] the following thermal and athermal phenomena contribute to the efficient sintering of hard to sinter borides along with other ceramics when SPS technique is used:

"Thermal:

(1) high heating rates, which enable powder systems' higher sinterability;

(2) high local temperature gradients, which provide conditions for thermal diffusion;

(3) highly nonuniform local temperature distributions, which cause local melting within interparticle contact areas; and

(4) highly nonuniform macroscopic temperature distributions, which create thermal stresses intensifying dislocation creep.

Athermal:

(1) electromigration and intensified diffusion in ionic conductors;

(2) electroplasticity mechanisms;

(3) ponderomotive forces;

(4) electromagnetic ''pinch'' effect; and

(5) dielectric breakdown of oxide films (cleansing effect) and defect generation at grain boundaries."

A schematic presentation of the SPS assembly is presented in Figure 6, where boride powder is located between two punches in a graphite die. The procedure is usually performed inside of a vacuum chamber, but argon or nitrogen environment can also be used, depending on the powder composition. The SPS process starts with an application of pulsed current. The heating process in SPS occurs by passing a current, such as pulsed DC goes through the die and the sample, if the sample is a conductor. The pressure is applied externally according to the predefined sintering route. The application of the current for the heating allows to achieve high heating rates, that have significant effect on sinterability. The schematic presentation of the SPS set up is shown in Figure 6. At this time, SPS is the most promising and well-developed technique to sinter boride ceramics, which was used in the presented research.

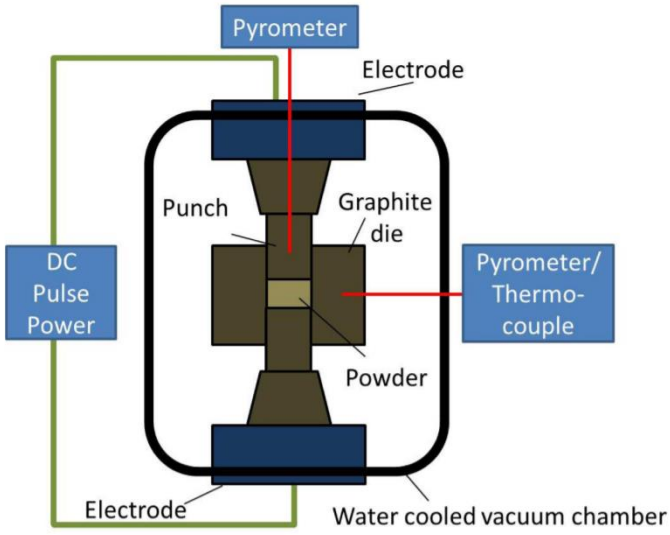

Figure 6 A schematic presentation of Spark Plasma Sintering (SPS) process [44]

Flash Spark Plasma Sintering (FSPS)

The Flash Spark Plasma Sintering Technique (FSPS) was introduced by the researchers at Queen Mary University of London and it allows to densify the material ultra-rapidly in a matter of seconds [45], [46], [47], [48], [49]. This densification of the material during FSPS happens due to high electric current that goes through sufficiently conductive sample developing ultra-fast heating rate up to 10 000 ˚C/min which dramatically reduces the time spent for the powder consolidation to 5-15 seconds. The voltage, which is being applied for the FSPS process, is ranging around 50-150 volts or even higher, as compare to the conventional Spark Plasma Sintering process where the voltage is less than 10V, which allows increase the heating rates during the FSPS dramatically [48]. A schematic of FSPS assembly is presented in the Figure 7, which closely resemble the assembly used in conventional SPS.

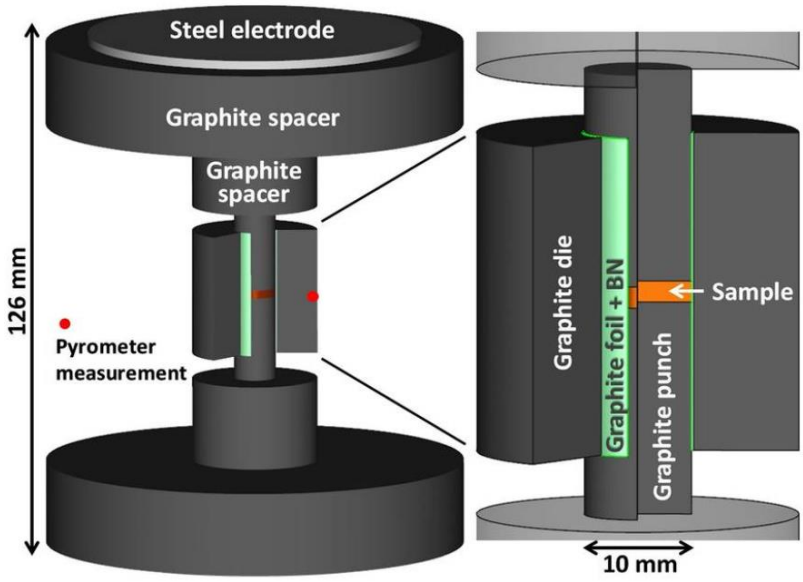

Figure 7 A schematic of Flash Spark Plasma Sintering (FSPS) [49]

As an example, in [45] it was reported that the densification of SiC/B_4C happened in just 2-3 seconds of discharge time from a powder mixture. Depending on a size of a graphite die as well as the desired sample size the FSPS time may take up to 60 seconds [48], [49].

Crystal Structure and Mechanical Properties of B_4C

Density

As B_4C ceramics consist of the very light B and C elements of the periodic table, and it has a very low density. Its density varies in the range of 2.46 g/cm^3 for $B_{10.4}C$ to 2.52g/cm^3 for B_4C and is determined by the stoichiometry of the compound increasing linearly with increasing carbon content where slightly different stoichiometry is defined by either excess B or C [50], [51]. The following linear equation which relates B_4C density and its carbon content was presented in [19]: $\rho(g/cm^3) = 2.422 + 0{\cdot}0048[C]$ at. %.

Crystal Structure

The crystal structure of B_4C consists of 12- atom icosahedra units located at the vertices of a rhombohedral lattice $R\bar{3}m$ space group, with 3–atom linear chains that link the icosahedra along the rhombohedral axis [4], [52], [53]. A schematic presentation of B_4C lattice is shown in Figure 8.

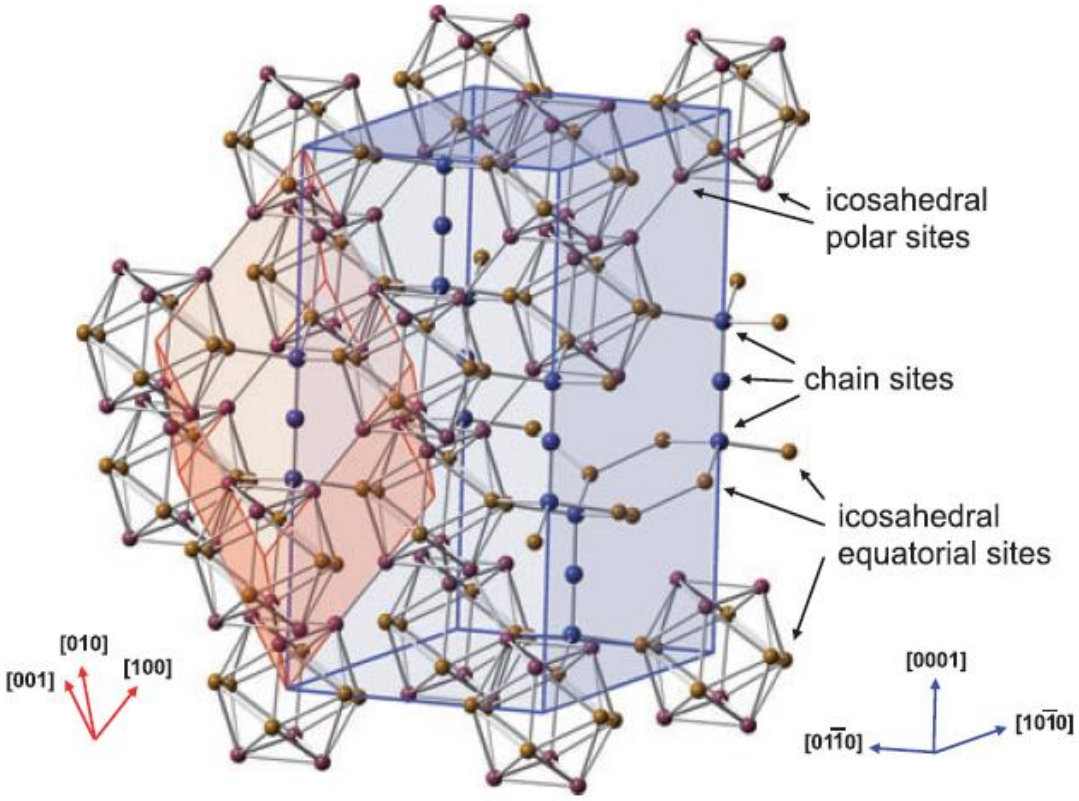

Figure 8 B_4C lattice describing the correlation between the rhombohedral (red) and the hexagonal (blue) unit cells [4]

The reported rhombohedral lattice parameters of carbon-rich B_4C are a = 5.16 A˚ and α = 65.7 A˚, or, if represented as a hexagonal lattice, its lattice parameters become a_0 = 5.60 A˚, c_0 = 12.07 A˚ with an axial ratio of c_0/a_0 = 2.155 [19], [54], [55]. The correlation between lattice parameters and stoichiometry of B_4C was established in [56]. The hexagonal lattice parameters and resulting unit cell volume versus B_4C composition is shown in Figure 9 [19].

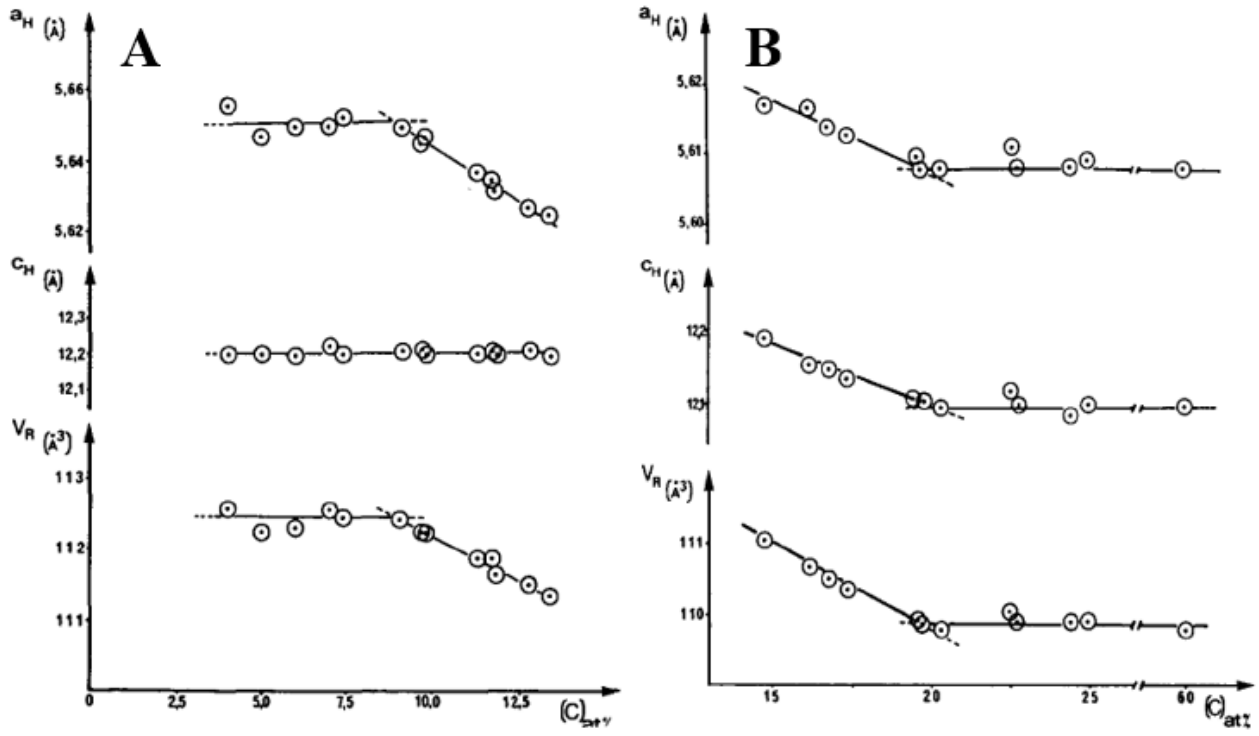

Figure 9 Hexagonal and lattice parameters and cell volume of boron-rich solids (A) and carbon-rich phases (B) [19]

The $R\bar{3}m$ B_4C structure implies the existence of four types of the atomic bonding – the interchain bonds, the chain icosahedral bonds, the intericosahedral bonds and the highly delocalized intraicosahedral sp_2 bonds [4]; and their localization and delocalization, ionicity and covalent character along with the electron density determine the properties of B_4C [55], [57], [58], [59]. As the atomic bonding in B_4C is very strong, the thermal expansion was measured as not very high and equal to $\alpha = 5.73 \times 10^{-6}$ K^{-1} for 300-1970 K in [60], 9.5×10^{-6} K^{-1} in [61] or 4-8 $\times 10^{-6}$ K^{-1} in [62]. The following equation was used to determine CTE: $\alpha = 3.016 \times 10^{-6} + 4.30 \times 10^{-9}t - 9.18 \times 10^{-13} t^2$ (t˚C) in [19].

It was established that B_4C is a p-type semiconductor with a rather small band gap of 1.64 eV [63]. Different band gap values of B_4C were also reported ranging from 0.48eV to 2.41eV [64], [65], which is a function of B_4C stoichiometry. B_4C was found to be a semiconductor over the entire homogeneity range, where its electric properties dominated by the hopping transport [66], [67], [68].

Lattice Dynamics and Vibration Properties

For lattice dynamics and vibrational properties group theory predicts $5A_{1g} + 2A_{1u} + 2A_{2g} + 6A_{2u} + 7E_g + 8E_u$ representation for the normal modes of lattice dynamics of $R\bar{3}m$ rhombohedral B_4C, where the 12 modes of A_{1g} and E_g symmetry are Raman active, the 14 modes of A_{2u} and E_u symmetry are IR active, and the A_{1u} and the A_{2g} modes are optically inactive. When the zero-frequency modes are removed, the number of IR active modes become 12 [69]. If carbon atoms are introduced into the icosahedron, a higher number of vibrational modes can be expected in the collected spectra [4]. Raman active mode at 480cm^{-1} arises from chain rotation perpendicular to the (111) plane, and the Raman active E_g mode at 535 cm^{-1} is due to the libration of the ($B_{11}C$) icosahedron. In another work [69] the Raman active A_{1g} mode of B_4C at 1080 cm^{-1} originated from the breathing vibration of the (B_{12}) icosahedron; an IR active E_u mode at 1040 cm^{-1} resulted from complex atomic displacement due to chain bending and antisymmetric stretching of B_{12} icosahedron; an IR active E_u mode at 487 cm^{-1} appeared from chain bending; a Raman active E_g mode at 335 cm^{-1} appeared from displacement of atoms due to chain rotation and wagging of an icosahedron; E_g Raman active mode at 172 cm^{-1} originated from rotation of an B_{12} icosahedron. The detailed description and analysis of Infrared and Raman active lattice vibrations is presented in [4]. Very recently, it was convincingly shown that the most reported spectra of B_4C stem from

surface phonon scattering directly related to the surface penetration depth of the laser as such the surface measurements brought a lot of controversy into the peak assignment of the bulk materials, because the energies of the laser used for these multiple measurements exceeded the reported 2.41eV band gap of B_4C and thus are non-suitable for their intended application [65].

The reported amorphization of B_4C under shock loading was reported in [70]. Different results suggesting an appearance of phase transition upon dynamic loading were also reported in a number of publications [71], [72], [73], [74], [75], [76]. Structural transformation of B_4C was also studied by indentation techniques [77], [78], [79], [80], [81], [82] where large amorphization zones with appearance nano size grains of crystalline material were found with retained orientation indicative of highly anisotropic deformation of B_4C upon loading [79]. The recent work [83], [84], [85] indicated that the redistribution of polar C atoms is a mechanism responsible for the high pressure second order phase transition occurring in B_4C, which was assigned to occur at a stress of ~33GPa. It was determined that at this pressure, the B_4C changes radically its optical properties. While at ambient condition B_4C is opaque indicative of presence of significant number of defects in the structure, however, it become extensively transparent at high pressure, which was correlated to the high pressure phase transition [86], [85]. Appearance of optical transparency upon phase transition implies disappearance of structural defects that determine electronic properties of semiconducting B_4C at ambient conditions. However, the lattice parameters of B_4C did not change significantly upon transition indicating that the phase transition is a second order. It was also determined that while X-ray or neutron diffraction cannot be used to study the minor structural change of B_4C phase, however, it was found that phonon spectroscopy is one of the best techniques to study such changes in the lattice [87].

Elastic Properties

As it was determined by numerous groups in the past mechanical properties of B_4C are derivatives of atomic bonding characteristics such as covalent vs ionic nature of the bonds, electron density in interatomic regions, as well as localization and delocalization of electrons in the structure. It was determined, that, indeed, B_4C bonding is responsible for its low compressibility, high stiffness and very high hardness. Due to the presents of anisotropy in atomic lattice, it was shown both by theoretical calculations [88] and experimental measurements [89] that the C_{11} elastic constant of B4C is higher than the C_{33} constant. The resonant ultrasound spectroscopy was used to study the anisotropy boron carbide elastic properties on $B_{5.6}C$ single crystal [89]. It was found that Young's modulus is indeed orientation dependent and has a E_{max} value of 522 GPa and E_{min} = 64 GPa, thus showing an anisotropy ratio of E_{max}/E_{min} = 8.1. The E_{max} was found to be aligned with the (111) direction thus implying higher stiffness of the crystal to tension or compression loading. Shear modulus measured on the (111) plane of $B_{5.6}C$ single crystal was found to be 165 GPa, however, when measured parallel to the (111) direction on pyramidal and prismatic planes it varied from 165 GPa to 233 GP, with 233 GPa maximum values measured along the (201) direction. The shear modulus anisotropy G_{max}/G_{min} = 1.4. The orientation dependence of the Young's and shear moduli of $B_{5.6}C$ single crystal is shown in Figure 10 and Figure 11. When polycrystalline B_4C ceramics is processed, it has isotropic mechanical properties due to overlapping of crystallographic orientation in multiple single crystal grains. Therefore, unless texture is intentionally introduced during processing, elastic properties of B_4C are independent of the directions. The longitudinal (V_L) and shear (V_S) ultrasonic waves velocities propagated in B_4C ceramics at RT are shown Table 1.

Table 1 Paramethers related to elastic properties of pollycrystalline B_4C [90]

Description	This work	Ref.[a]	Ref.[b]	Ref.[c]
Density ρ (kgm^{-3})	2514 ± 15	2500	2550	2510
Longitudinal velocity V_L (ms^{-1})	14086 ± 12	13780	14166-14205	
Shear velocity V_S (ms^{-1})	8766 ± 7	8540	8851	
Longitudinal stiffness C_L (GPa)	498 ± 4	475		
Shear stiffness μ (GPa)	193 ± 1	182	200	
Bulk modulus B^S (GPa)	240 ± 3	232	247	
Young's modulus E (GPa)	456 ± 4	434	472	461
Poisson's ration	0.18 ± 0.004	0.188	0.18	0.178
Acoustic Debye temperature Θ_D (K)	1480 ± 3			
$(\delta C_L/\delta P)_{P=0}$	5.70 ± 0.3			
$(\delta \mu/\delta P)_{P=0}$	0.78 ± 0.04			
$(\delta B^S/\delta P)_{P=0}$	4.67 ± 0.3	4.2 ± 50%		
γ_L	1.21 ± 0.07			
γ_S	0.33 ± 0.02			
γ^{el}	0.62 ± 0.03			
γ_{th}	1.76			

Where a – [91]; b – [92], [93]; c - [94].

It was found that shear wave velocities measured parallel and perpendicular to one principal axis were identical, which was an indicative of absence of preferred orientation in the isotropic polycrystalline B_4C. Two independent elastic stiffness moduli values $C_L = \rho V_L^2$ and $\mu = \rho V_S^2$ are also presented in Table 1. Besides, the adiabatic bulk modulus B^S, Young's modulus E, Poisson's ratio ν, and the acoustic Debye temperature were all calculated from ultrasound velocity and B_4C sample density in [90]. In addition, the comparison of parameters between different measurements is also given in Table 1.

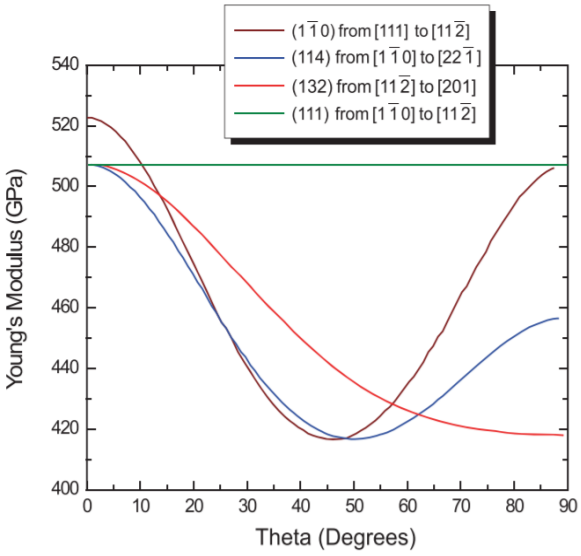

Figure 10 Young's modulus orientation dependence of $B_{5.6}C$ single crystal [4]

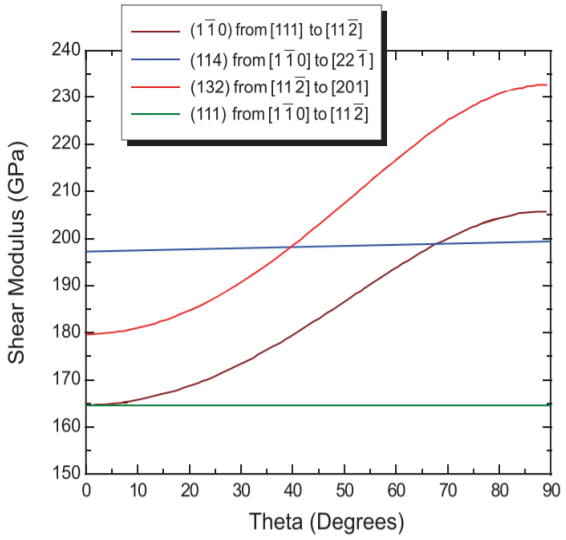

Figure 11 Shear modulus orientation dependence of $B_{5.6}C$ single crystal [4]

Typically, Young's modulus values of dense B_4C ceramics, measured by acoustic techniques are reported to be in the range of 460 - 470 GPa [3], [95], however, a higher value of 570 GPa was also reported for 100% dense B_4C [96]. The elastic properties of B_4C was also reported in [90],

where Young's modulus value was found to be equal to 456 ± 4 GPa, bulk modulus was equal to 240 ± 3 GPa and Poisson's ratio was determined to be equal to 0.18 at room temperature. The elastic properties of B_4C in [90] was studied over 150 - 300K temperature range and the results are shown in Figure 12. The range of Poisson's ratio values of B_4C was also reported to be in range between 0.17 – 0.21 in [19], [97], [4].

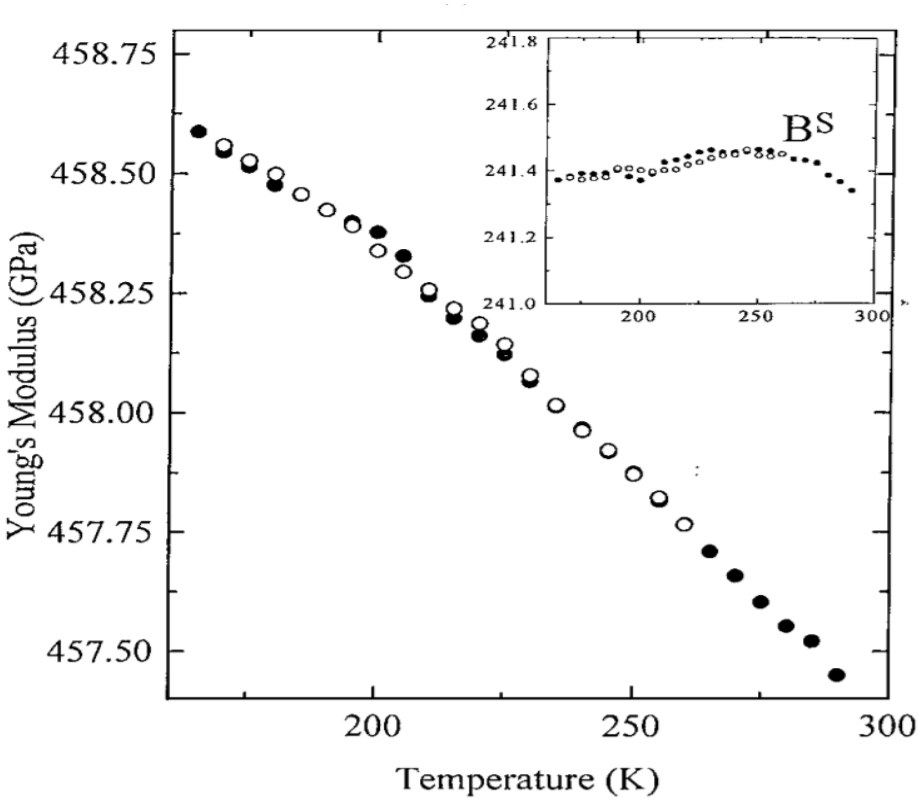

Figure 12 Young's modulus of B_4C as a function of temperature with an insert of the values of bulk modulus (B^s) [90]

The stoichiometry of B_4C will affect its elastic properties [19] and selected data for elastic moduli and Poisson's ratio of polycrystalline samples of B_4C with different amount of carbon are shown in Table 2.

Table 2 Elastic moduli and Poisson's ratio dependence of boron carbide composition [4]

Stoichiometry	at. % C	Bulk modulus GPa		Young's modulus GPa	Shear modulus GPa	Poisson's ratio
		Exp.	Calc.	Exp.	Exp.	Exp.
B_4C	20	247[c]	246[e]	472[c]	200[c]	0.18[c]
		235[e]	234[g]	462[e]	197[e]	0.17[e]
		199[d]	248[h]	448[b]	188[a]	0.21[b]
			239[j]	441[a]		
			220[a]			
$B_{4.5}C$	18.2	237[c]		463[c]	197[c]	0.17[c]
$B_{5.6}C$	15.2	236[c]		462[c]	197[c]	0.17[c]
		237[f]		460[f]	195[f]	0.18[f]
$B_{6.5}C$	13.3	231[c]	217[g]	446[c]	189[c]	0.18[c]
			227[i]			
$B_{7.7}C$		178[c]		352[c]	150[c]	0.17[c]
B_9C		183[c]		319[c]	150[c]	0.21[c]
		130[c]		348[c]	132[c]	0.16[c]

Where, a - [98], b - [99], c - [100], d - [101], e - [97], f - [89], g - [88], h - [51], i - [57], j - [102].

Hardness

Elastic properties of B_4C, such as Young's modulus, shear and bulk moduli along with the Poisson's ratio determined mostly by internal properties of the crystal lattice determined by the bonding withing structure. Presence of porosity will significantly affect the elastic properties of B_4C significantly decreasing them even with an insignificant increase in the porosity. Hardness of B4C, similar to Young's modulus, is also very high because of the presence of strong covalent bonding. Knoop hardness was reported to be in the range of 28 – 31 GPa [19], while Vickers hardness was reported to vary in a much broader rang e of 32 – 42 GPa, depending on the

stoichiometry of B_4C as well as the applied load used in measurements [103], [104], [105]. Vickers hardness as a function of the grain size was measured in [106], where the hardness value decrease significantly when the average grain size increased from 2.2 μm to over 3 μm (Figure 13).

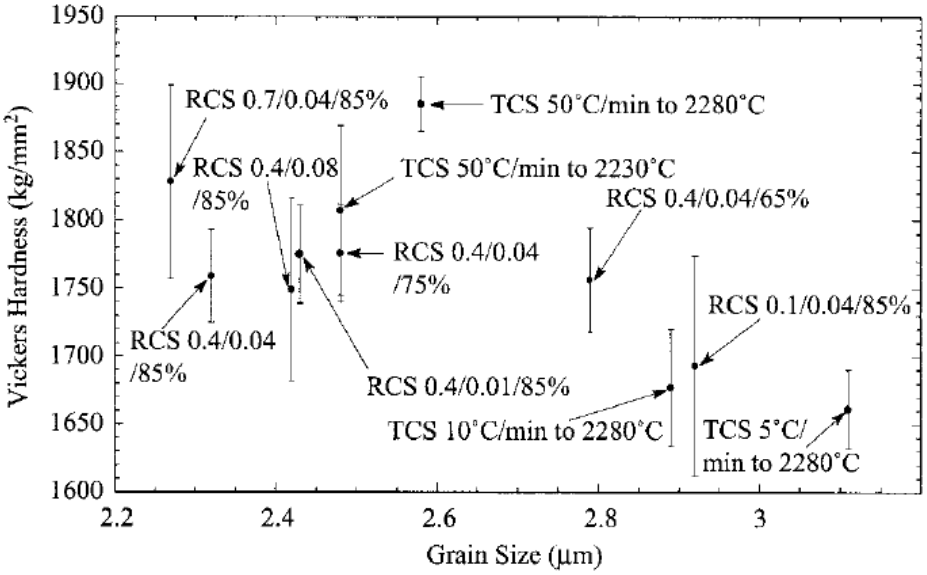

Figure 13 Vickers Hardness of pressureless sintered B_4C as a function of grain size. Labels depict the sintering techniques, RCS is rate-controlled sintering and TCS is temperature control sintering

It is recognized that the hardness strongly depends on grain size, porosity, purity, stoichiometry, presence of defects, loading conditions, etc. For example, the hardness of B_4C measured using nanoindentation were consistently reported as being 41 - 42 GPa [77], [78], but it could reach much higher values of 50 GPa and above, due to indentation size defects that become negligibly small or vanish at testing by Vickers indenters where loads are much higher [107]. Different groups also reported that hardness of B_4C increases when carbon content increased till the end of the homogeneity range [108], [78], [109], [110]. Nanoindentation hardness of B_4C single crystals or polycrystalline ceramics was reported to be around 39-55 GPa as measured using a Berkovich

indenter [77], [111], [104]. While no discontinuities were observed during nanoindentation of (111) surface of $B_{4.3}C$ single crystal (Figure 14) [4], discontinuities in the loading and unloading deformation plots of polycrystalline B_4C during nanoindentation were found (Figure 15), which were either explained by cracking or by the transition from elastic to elastoplastic deformation caused by homogeneous nucleation of dislocations due to the high shear stresses below the indenter [111].

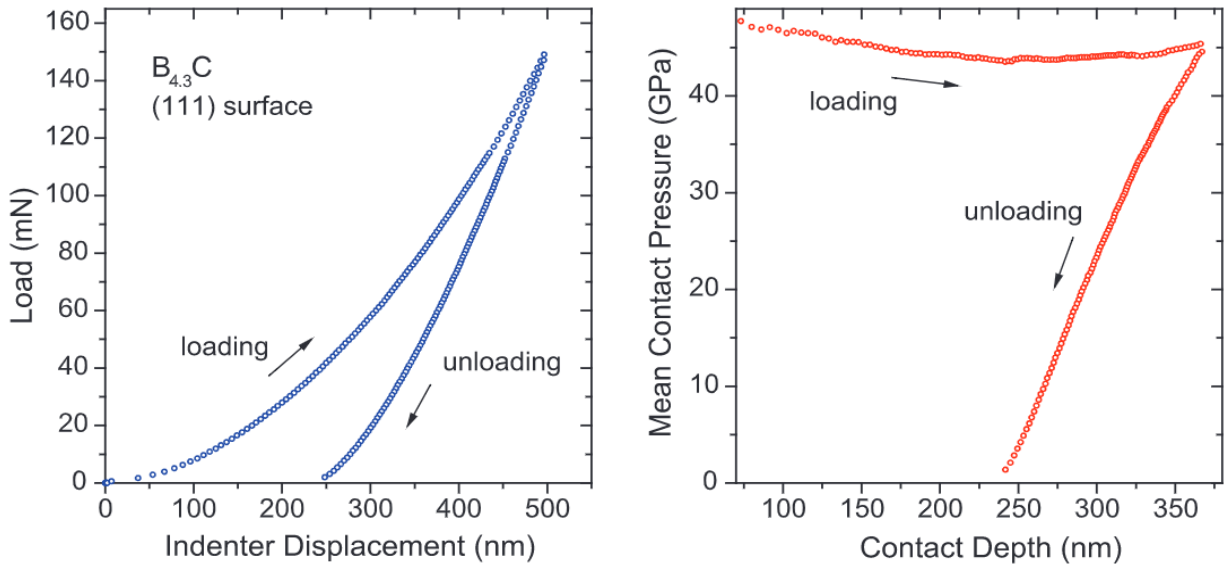

Figure 14 Load vs displacement and mean contact pressure vs contact depth curves of $B_{4.3}C$ on (111) surface [4]

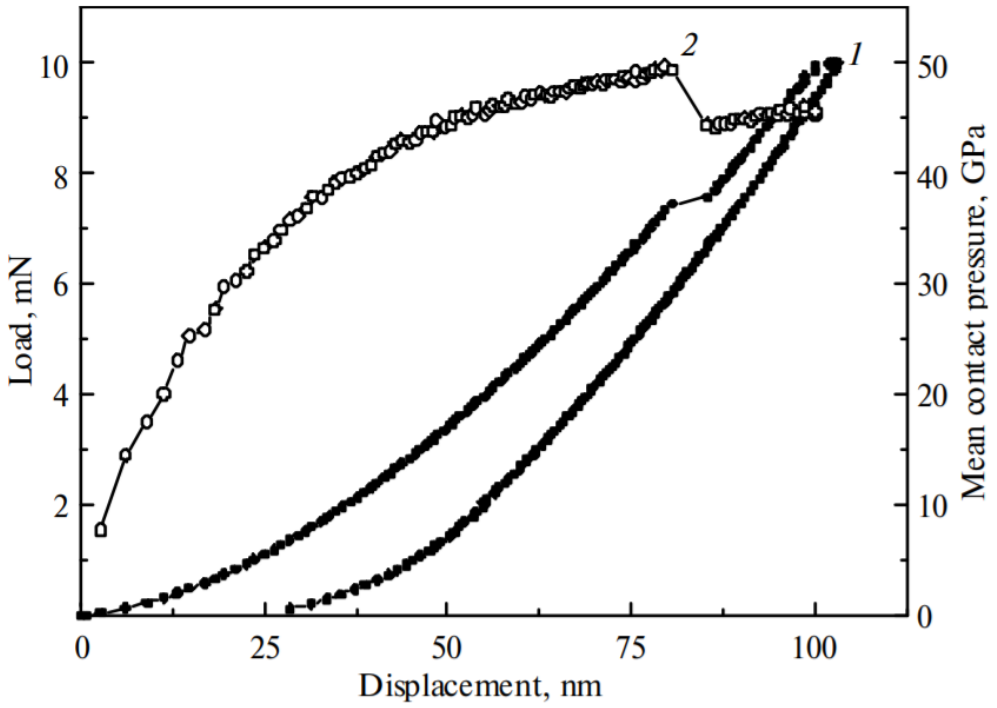

Figure 15 Load – displacement curve (1) and mean contact pressure (2) of B_4C [111]

A very strong covalent bonding of B_4C is responsible for high hardness and high Young's modulus, thus making it a perfect candidate for protective materials.

Strength and Fracture Toughness

Unlike elastic moduli and hardness, the 4-point bending flexural strength is relatively low and reported to be around 250 – 450 MPa [19], [112], [21]. However, the compressive strength is rather high and measured to be around 6.1 ± 0.3 GPa [113]. Both strength and Young's modulus strongly depend on density o B_4C and the related dependence is shown in Figure 16.

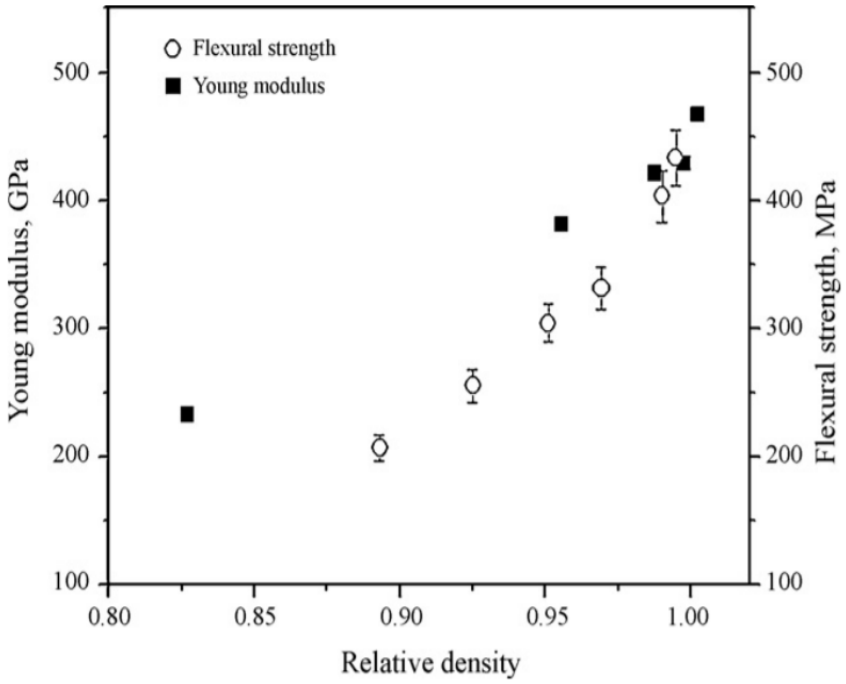

Figure 16 Flexural strength and Young's modulus as a function of relative density of B_4C [114]

Similar to hardness, the strength of B_4C strongly depends on processing condition leading to the presence of porosity and other defects, as well as grain size As such, the B_4C strength could be significantly increased if the processing conditions are improved leading to formation of dense material with reduced number of the defects that also have small size. Improved techniques, such as SPS or even FSPS could lead to processing of ceramics with significantly enhanced stress-strain deformation behavior of B_4C. The major problem of B_4C ceramics is that, as the majority of all ceramic materials, it is very brittle [115]. Thus, K_{1c}, measured from the length of the cracks originated from the corners of Vickers impression and called indention crack resistance in some publications [105], [103] was reported to be in the range of 2 – 3.5 MPa · $m^{1/2}$, which varied slightly with the grain size of the B_4C (Figure 17). K_{1c} of B_4C was also measured using a variety

of different techniques, such as Single Edge V Notched Beam [116], Surface Crack in Flexure [117], and Chevron Notch Beam [118], where similar low values of K_{1c} were also reported.

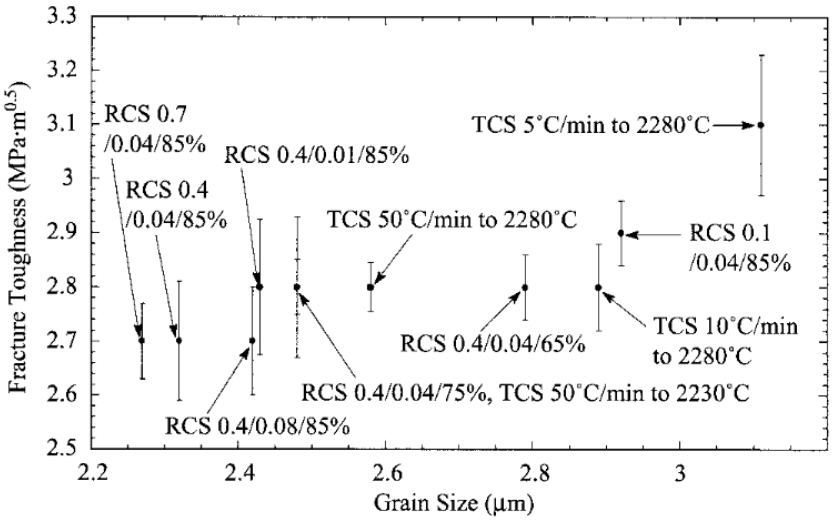

Figure 17 Fracture toughness as a function of grain size of pressureless sintered B_4C, RCS – rate-control sintering, TCS – temperature-controlled sintering [106]

CHAPTER 2: MATERIALS AND EXPERIMENTAL TECHNIQUES

R. Kuliiev, N. Orlovskaya, H. Hyer, Y. Sohn, M. Lugovy, D. Ha, M. Radovic, E. Castle, M. Reece, P. Warriam Sasikumar, L. Conti, G. Blugan, T. Graule and J. Kuebler, "Spark Plasma Sintered B_4C: Structural, Thermal, Electrical and Mechanical Properties," *Materials*, vol. 13, no. 7, 1612, 2020

Experimental

Processing

A commercially available B_4C Grade HD07 powder from H.C. Starck (Germany) with a particle size of 0.8 µm, specific surface area of 15 - 20 m^2/g and the B:C ration of 3.7 – 3.8 was used to sinter dense B_4C samples for flexural and biaxial testing. The 3x4x45mm and 2x2.5x25mm bars for bending experiments were cut and machined from a large 100mm diameter and 10 mm thickness disk sintered in a graphite die at 2150^oC, 40 MPa with a 10 minutes dwell time performed at Dr. Fritsch company, Germany. For the biaxial strength tests a 20 mm diameter graphite die was lined with graphite foil and charged with 2g of B_4C. The die was then placed into the Spark Plasma Sintering (SPS) furnace (FCTHPD25; FCT SystemeGmbH, Rauenstein,Germany) and heated at a rate of 100°C/min under a minimum pressure of 16 MPa to 1800°C, held for 10 min while the pressure was increased to 40 MPa, and then heated at 25 °C/min to 2150°C for a 10 min hold before cooling to room temperature over 20-25mins. The sintering regime for the B_4C disks is shown in Figure 18. The final density of the B_4C bars and disks after sintering was measured using Archimedes technique [119]. The sintering of B_4C disks was performed at Queen Mary University of London, the UK.

Structure

The crystal structure of B_4C ceramics was studied using an X-ray diffractometer (XRD, Bruker-AXS D8 Advanced Bragg-Brentano X-ray Powder Diffractometer, Bruker, WI). Raman spectra of B_4C ceramics were collected using a Renishaw InVia Raman microscope (Renishaw Inc., Gloucestershire, UK). The Raman microscope system comprises a laser (532nm line of solid Si) to excite the sample, and a single spectrograph fitted with holographic notch filters. Before collecting spectra, the spectrometer was calibrated with a standard silicon wafer using the Si band position at 520.3cm^{-1}.

The average collection time for a single spectrum was 30s, and the spectrum was collected from the polished surface of sintered B_4C sample. Thermal expansion measurements were carried using a thermal mechanical analyzer (NETZSCH TMA 402F3, Germany) in the temperature range of 30 to 1000 °C with a heating rate of 5 °C/min. The load was set to 0.1 N and the average linear coefficient of thermal expansion was determined from the obtained thermal expansion data. Room temperature DC electrical resistivity of the 4x3x45mm bars was measured using a 4-probe experimental set up connected to a Keithley 2450 source meter (Textronix UK, Ltd, Berkshire, UK). A potential difference of 1V was applied through the outer probes and the corresponding current between the inner probes was measured for calculation of the resistance values.

Elastic Properties

The Impulse Excitation Technique (IE, Grindo-SonicMk5“Industrial” J.W. Lemmens, Belgium), was used to determine the elastic modulus of the B_4C bars at room temperature, and the measurements were carried out in accordance with the EN843-2 standard [120]. Samples, in the form of 3x4x45mm bars of known density, were lined up with a supporting cylinder and placed

over a microphone. To determine the elastic modulus at room temperature using the natural frequency of vibration of the bars, they were struck lightly using a small hammer and the acoustic vibrations were recorded using the microphone. Then, using the dimensions of the sample, its density and natural frequency of vibration, the Young's modulus was calculated.

In addition to the IE measurement, the Young's and shear moduli of B_4C were also measured using a Resonant Ultrasound Spectroscopy technique using a custom made high-temperature resonant ultrasound spectroscope (HT-RUS) that utilizes a commercially available room temperature (RT) RUS (Magnaflux Quasar, Albuquerque, NM) system. RUS is a high-precision dynamic technique, which is used to determine the elastic moduli and energy dissipation (mechanical damping) of materials by measuring the vibrational spectrum of samples with well-defined geometry, usually in the shape of parallelepipeds or cylinders [121], [122], [123], [124]. A B_4C sample in the form of disc with 20mm diameter and 1.5mm thickness was supported by three piezoelectric transducers. One transducer, which is a transmitting transducer, generates an elastic wave of constant amplitude, but of varying frequency covering a large number of vibrational eigenmodes of the sample. The resonance response of the excited sample is detected by the other two transducers, which are receiving transducers. To study the elastic moduli as a function of temperature, SiC extension rods were added to transmit the ultrasound waves to the RT RUS equipment. This arrangement allowed the B_4C disk to be held on the tip of the extension rods, at the desired temperature in the furnace, while the transducers were unaffected by high temperature. The measurements were performed under vacuum. The B_4C sample was heated at a rate of 10°C/min and resonance spectra were collected at an interval of 25 °C up to 1000°C after an isothermal hold of 20 min. Depending on the density and stiffness of the material, measurements

were done in the 20–500 kHz frequency range to cover the first 40 frequencies. The RUS spectra cannot be de-convoluted directly to deduce the elastic constants. Starting from the known sample dimensions, density, and a set of "guessed" elastic constants—namely C_{11} and C_{44} for an isotropic solid, where C_{11}=542,8 GPa and C_{44}=164.8Gpa as reported in [125], the elastic moduli were determined from collected RUS spectra using a multidimensional algorithm (MagnafluxQuasar, Albuquerque, NM) that minimizes the root-mean-square (RMS) error between the measured and calculated resonant peaks.

Nanoindentation

Nanoindentation of B_4C was performed using a Hysitron TI Premier machine equipped with a Berkovich tip. A total of 25 indents were produced on the polished surface of B_4C samples using a maximum load of 9500 μN, which was held for 3 seconds at the maximum load between loading and unloading. Load vs. displacement curves were analyzed to calculate the hardness, H, and reduced modulus, E_r, using a method described by Oliver and Pharr [126], [127].

The mean contact pressure was calculated as

Equation 1: Mean contact pressure

$$p_i = \frac{P_i}{A_i}, \tag{1}$$

where P_i is the instantaneous indentation load taken from the corresponding load – displacement diagram (P_i may be taken directly from indentation data points); A_i is the contact area, which is determined using the area function:

Equation 2: Contact area

$$A_i = C_0(h_c)_i^2 + C_1(h_c)_i + C_2(h_c)_i^{1/2} + C_3(h_c)_i^{1/4} + C_4(h_c)_i^{1/8} + C_5(h_c)_i^{1/16}, \quad (2)$$

where C_0, C_1, C_2, C_3, C_4, andC_5 are the coefficients determined for a given indenter from a series of indents at various contact depths in a sample of known elastic modulus (typically fused quartz). Note that C_0=24.5 for an ideal Berkovich probe; $(h_c)_i$ is the contact depth corresponding to P_i , which can be calculated as

Equation 3: Contact depth

$$(h_c)_i = h_i - (h_e)_i, \quad (3)$$

where h_i is the total measured indenter displacement corresponding to P_i (h_i may be taken directly from indentation data points); $(h_e)_i$ is the corresponding elastic deflection [128], [129], [130]:

Equation 4: Elastic deflection

$$(h_e)_i = (h_e)_{max}^{\frac{P_{max}}{S\sqrt{\frac{P_i}{P_{max}}}}\sqrt{\frac{P_i}{P_{max}}}}, \quad (4)$$

where $(h_e)_{max}$ is the elastic deflection at maximum load P_{max} of the indentation diagram; the unloading stiffness S is the slope at the beginning of the unloading portion of the indentation diagram; ε is a constant that depends on the indenter's geometry (ε =0.75 for Berkovich indenter). After calculation, the mean contact pressure can be plotted against the contact depth.

The B_4C sample surface was first ground and further polished down to a 1 mm diamond grit size to determine the Vickers hardness of the ceramics. A Vickers hardness tester Durimet (Ernst-Leitz, Germany) was used for hardness tests in accordance with EN843-4 standard. The hardness of the samples was measured using a 9.8 N load applied for a period of 15 s. Twenty impressions were produced for the measurements of the sizes of the impression diagonals. The hardness H (GPa) was calculated according to the equation [131].

Equation 5: Hardness

$$H = 1854 \frac{P}{d^2} \quad (5)$$

where P is the indentation load in N, and d is the impression diagonal length in μm.

Strength of B_4C

Four-point bending tests were performed to measure flexure strength using B_4C samples with dimensions of 2x2.5x25 mm. To obtain load-displacement bending diagrams, the B_4C samples were loaded using a four-point bending jig with 3 mm diameter rollers with a 10 mm loading span and 20 mm supporting span using a 2 kN load cell on an universal testing machine (Zwick, Germany) in accordance with the EN 843-1 standard [132].

The biaxial strength of B_4C samples were tested using a ring-on-ring testing jig [133]. Disks with 20mm diameter and 1.5mm thickness were placed on the support ring and loaded with a loading ring in load control mode with a loading rate of 80N/s or 22MPa/s until failure of the disk occurred. The disks were polished on one side, and the polished surface was on the tensile side of the ring-on-ring fixture. The recorded load was recalculated into stress using the ASTM Standard C1499

equation [134]. As the deflection of the disk was not recorded during loading, the deformation of the B_4C samples was calculated using the measured Young's modulus in the elastic beam equation, as it is well known that B_4C behave elastically and does not show any plasticity during static deformation at room temperature [135], [136]. A standard Weibull analysis of strength data was carried out [137], [138], [139], [140].

Finite Elements Analysis (FEA) of the Stress Distribution for Biaxial Model

Finite Elements Analysis (FEA) modeling of the biaxial strength testing of B_4C was performed using the functions of the Simulia Abaqus® 6.11-1 software (Dassault Systems, Vélizy-Villacoublay, France). The B_4C specimen was treated as a deformable body and the loading/supporting rings as discrete rigid bodies. Load and support rings were defined as a 2D axisymmetric and homogenous model, with properties of 4140 alloy steel. The sample was defined using properties t obtained experimentally from the B_4C biaxial strength tests. The elastic modulus and the Poisson's ratio for a B_4C sample were taken as 429 GPa and 0.185 and for 4140 alloy steel were taken as 200GPa and 0.29, respectively. The contact between the specimen and ring-on-ring surfaces were defined as surface-to-surface contacts with a master surface on the rings. The simulation was performed with a friction of 0.1. In order to conduct a simulation, a support-ring was fully fixed in its position in any direction, however the loading ring was fully fixed besides the direction of the force in the Y-axis. The experimental data showed that the sample broken at a load of 1530N, therefore the force for the simulation for the loading ring was chosen to be 1530N in order to simulate a uniform pressure along the load-ring surface area. The mesh element type was defined as Discrete Rigid Element (RAX2) and for the sample as an Axisymmetric Stress (CAX4) with a reduced integration. The size of the mesh for a sample was chosen to be 0.2 mm

and 0.1mm for the loading and supporting rings. Therefore, after a successful simulation run it was found that the maximum tensile biaxial stress occurred along the bottom surface of the specimen, presented by a red area in Fig. 10, with a value of 436.1 MPa.

Fracture toughness was measured using the Single Edge V Notch Beam (SEVNB) technique in accordance with the CEN/TS 14425-5 standard [141]. A single notch was made on the 3 mm side of the $3 \times 4 \times 45$ mm^3 bar as near to the center as possible with a depth between 20 and 40% of the total thickness of the bar, since it was shown that within this range the depth of the notch has no influence on the measured K_{1c} values [142]. A diamond saw was used to make the initial 0.5 mm depth notch; after that the final 1–1.5 mm depth notch with ~1.8-2.2 μm tip radius was produced by machine cutting using a razor blade with 6 μm and then 1 μm diamond paste deposited. Three samples were tested at room temperature with a crosshead speed of 0.5 mm/min.

CHAPTER 3. B_4C PROPERTIES

Shrinkage behavior, structure, thermal expansion and electrical resistivity of sintered B_4C ceramics

Figure 18 shows the shrinkage of B_4C ceramic during Spark Plasma Sintering together with the pressure and temperature profiles, as a function of sintering time. The sample was heated from 400^{o}C to 1800^{o}C in 20 min under a minimal pressure of 16 MPa, then dwelled for 10 min during which a pressure of 40 MPa was fully applied, then the temperature was increased to 2150^{o}C and dwelled at this sintering temperature for 10 min before cooling down to room temperature. To protect the sample from fracture, the 40 MPa pressure was decreased at the beginning of the dwell time at 2150^{o}C in a such way that it reduced back to 16 MPa in 10 min by the end of dwell. As can be seen in Figure 18, expansion of the equipment was observed upon heating all of the way up to 1800^{o}C (region A, Figure 18) until the moment when the applied pressure was increased, causing shrinkage of the sample (region B, Figure 18). Under the constant pressure but with temperature increasing, most of the shrinkage of the B_4C sample occurred (section C, Figure 18). When the sample dwelled at 2150^{o}C, but with decreasing pressure, the shrinkage remained constant (section D, Figure 18), possibly because the majority of the densification process had already occurred. During cooling from the sintering temperature, shrinkage of the sample occurred (section E, Figure 18). After sintering, the samples were machined, surfaces polished, and the density was measured to be equal to 2.50±0.07 g/cm^3 showing less than 1% of porosity.

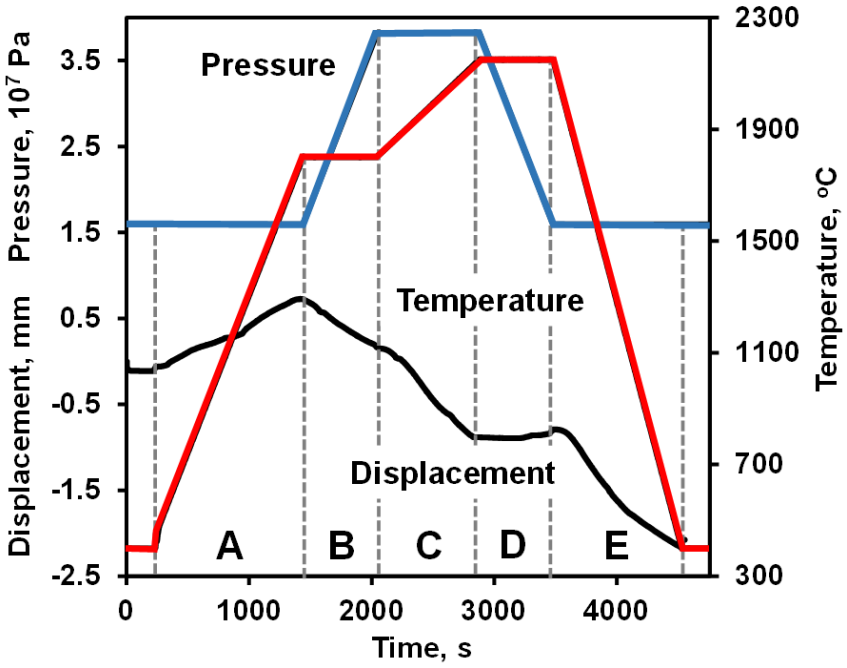

Figure 18. Pressure, temperature and shrinkage of B_4C densified by SPS.

An X-ray diffraction pattern taken from polished surface of B_4C is shown in Figure 20.

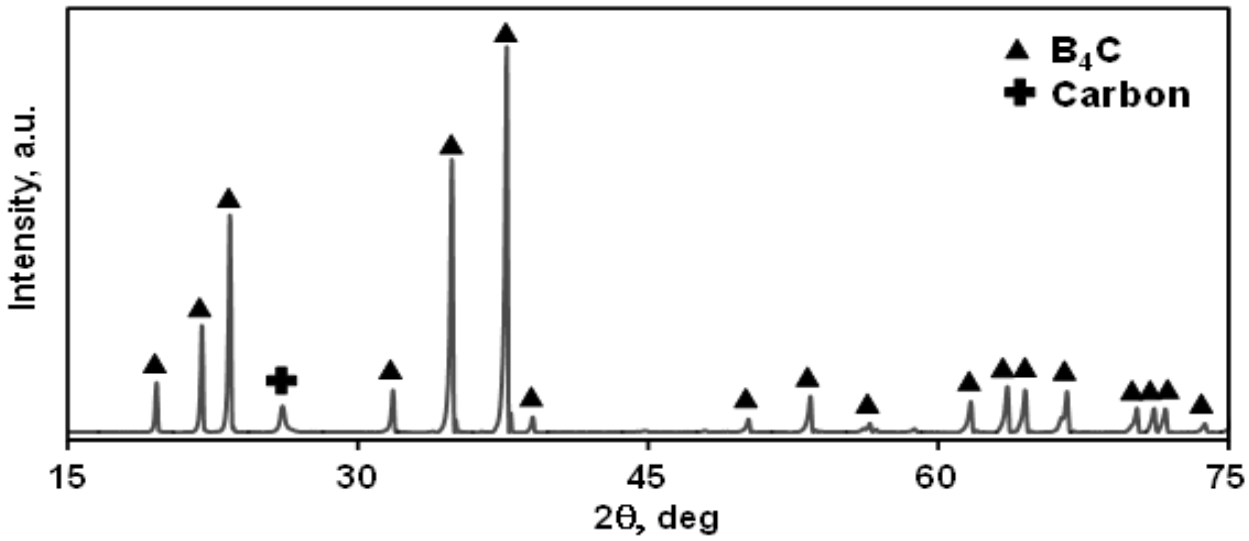

Figure 19 An X-ray diffraction pattern of B_4C

All of the diffraction peaks in the pattern belong to the rhombohedral Bravais lattice of $R\bar{3}m$ space group of B_4C, and the peak at ~26.16° 2Θ belonging to carbon indicates that a small quantity of carbon was present as a secondary phase [143], [144]. Raman spectrum obtained using a 532 nm laser measured from a polished surface of B_4C is shown in Figure 20. The spectrum resembles the surface spectrum of B_4C published in [65], [144].

The grain size of B_4C was equal to 3.4±0.05 micron as estimated from the fracture surface of broken samples (Figure 21). The thermal expansion of B_4C was almost linear, and the average coefficient of thermal expansion was calculated to be equal to $6 \cdot 10^{-6}$ / K in the 25-1000 ˚C temperature range (Figure 22). The measured values of CTE corresponded very well to previously published results, where the CTE of hot pressed B_4C was reported to be equal to 6×10^{-6} /K [145]. The room temperature DC electrical resistivity was measured to be equal to 0.00284 ± 0.0009 Ω m (Table 4), which is typical of the values reported for B_4C [63].

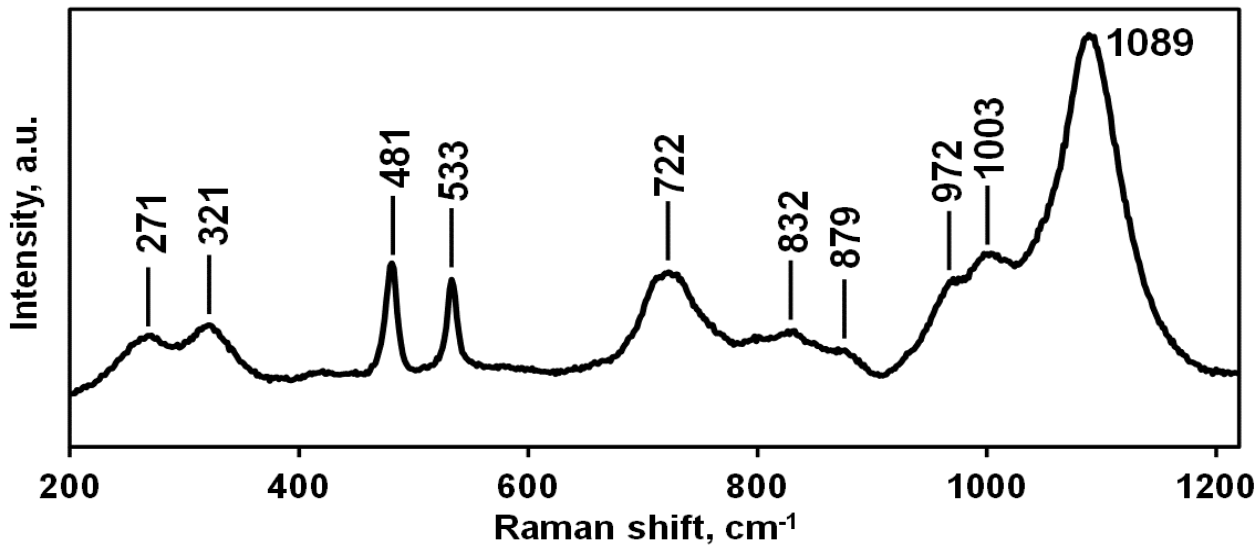

Figure 20. Raman spectrum of B_4C taken from polished surface.

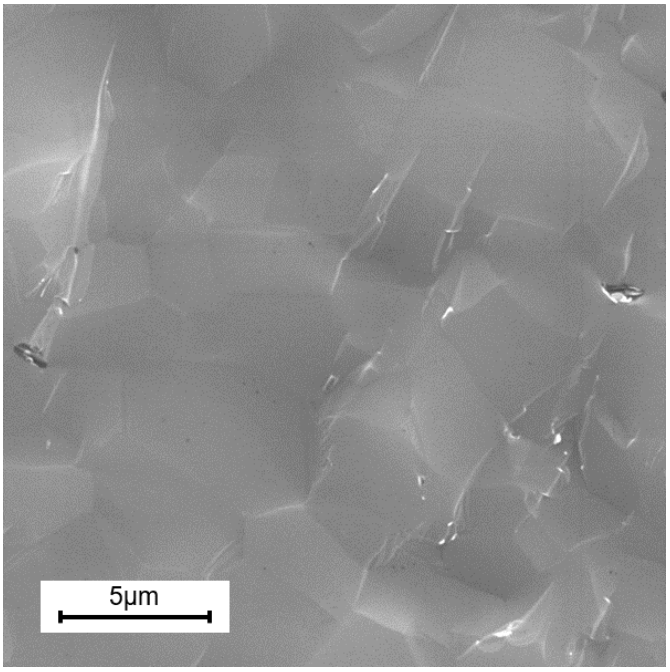

Figure 21. SEM of fracture surface of B_4C after flexture strength testing.

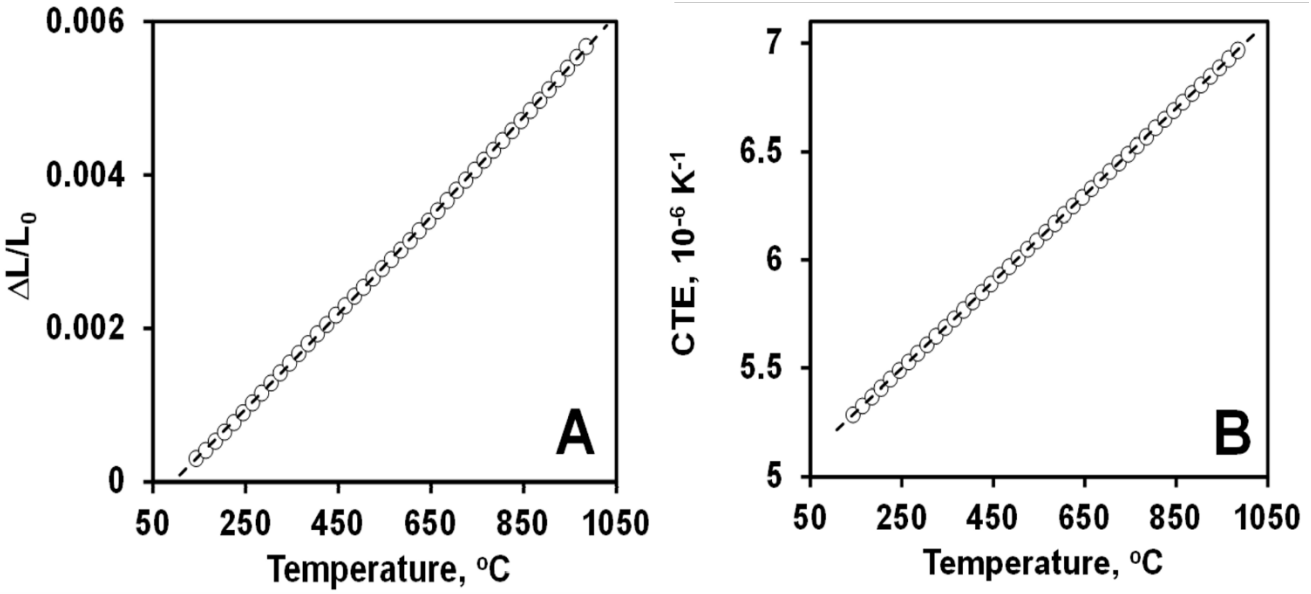

Figure 22. (A) Thermal expansion and (B) coefficient of thermal expansion of B_4C as a function of temperature.

Elastic properties of B_4C by Impulse Excitation (IE) technique and Resonant Ultrasound Spectroscopy

The Young's modulus of B_4C measured using the IE technique at room temperature was equal to 442±3 GPa (Table 4), which corresponds very well with the values of 440 to 560 GPa reported in other papers [146], [147].

The results of the measurements of Young's and the shear moduli along with bulk modulus and Poisson's ratio by RUS as a function of temperature are shown in the Figure 23B. The Young's modulus of B_4C measured by RUS was slightly higher compared to that measured using IE and was equal to 458.7 GPa at room temperature. The Young's modulus decreased linearly upon heating in in vacuum and was 436.7 at 1000˚C. The shear modulus, also measured by RUS, was equal to 195.7 GPa at room temperature, but slightly decreased linearly on heating to 186.5 GPa at 1000˚C. The bulk modulus and Poisson's ratio were calculated from Young's and shear moduli data and were equal to 220.9 GPa and 0.172 at 1000˚C. Note that Poisson's ratio of B_4C remains the same for the whole RT - 1000˚C temperature interval (Figure 23B). All of the values of elastic properties of B_4C presented in Figure 23 correspond very well with previously published data, where Young modulus was reported in the range of 440-560 GPa, shear modulus was reported in the range of 188-194 GPa, bulk modulus was reported in the range of 220-248 GPa and Poisson's ratio was reported in the range 0.19-0.21 [146], [147], [148], [96].

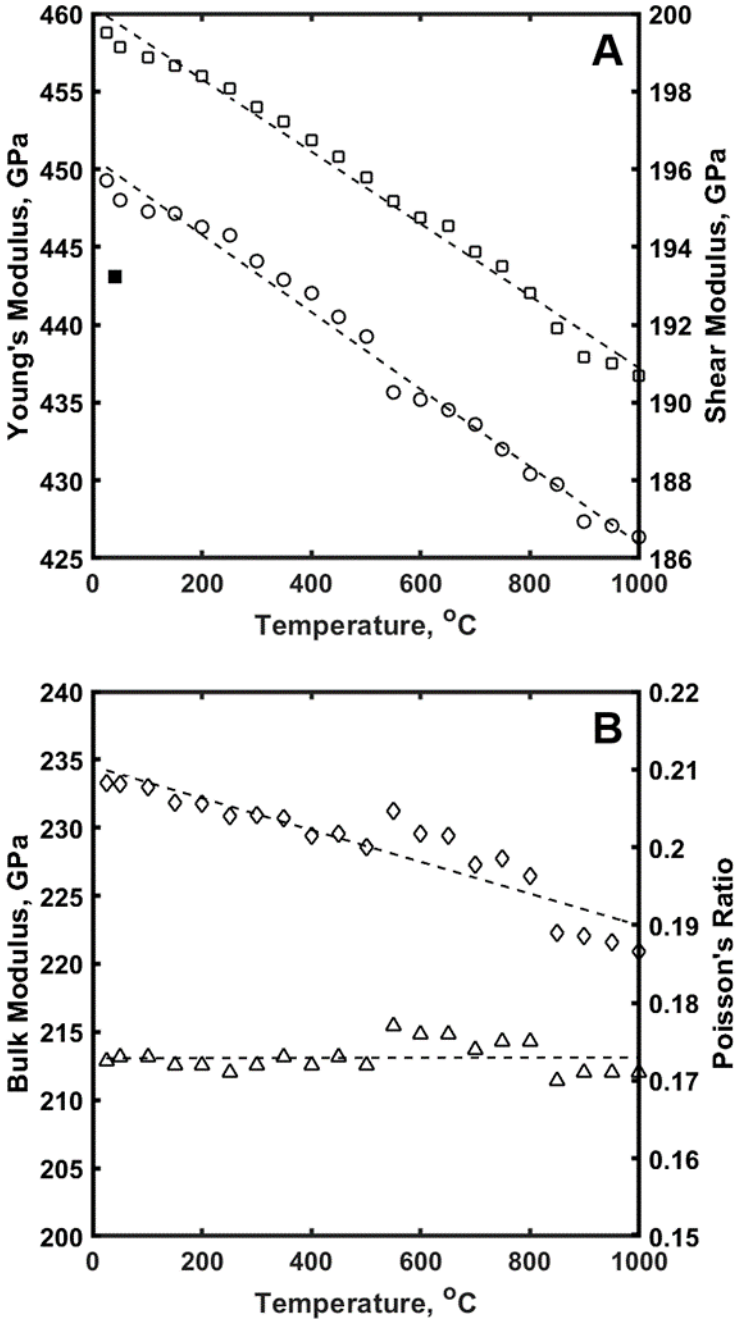

Figure 23. Elastic properties of B_4C measured by RUS. (A) Young's modulus (□) and Shear modulus (○) as a function of temperature: (B) Bulk modulus (◊) and Poisson's ratio (Δ) as a function of temperature. Young's modulus (■) measured by IE.

Young's modulus and nanohardness by nanoindentation and Vickers hardness by microindentation

The Young's modulus along with hardness of B_4C was also measured using the nanoindentation technique. Total 75 impressions were made into a polished B_4C surface using a Berkovich indenter. All measured values of nanoindentation hardness and Young's modulus are presented in the Table 3. The average values of Young's modulus and hardness were measured to be equal to 419.2 ± 47.3 GPa and 41.1 ± 5.7 GPa, respectively (Table 4). The Young's modulus values measured by nanoindentation are very similar to the ones measured by IE and RUS, but were slightly lower than the 506 GPa values, also measured by nanoindentation, reported in [149]. However, in [149] the reported high value of 506 GPa for the Young's modulus was measured on a single crystal in one specific crystallographic directions of (0001) and (10-11) respectively, thus the anisotropy of the bond strength in a certain crystallographic direction may explain this discrepancy. The average hardness value measured during nanoindentation was calculated to be equal to 41.1 ± 5.7 GPa, while the Vickers hardness measured using a microhardness tester was equal to 28.5±1.2 GPa (Table 4). The Vickers hardness impression after indention with a 1 kg load is shown in Figure 24.

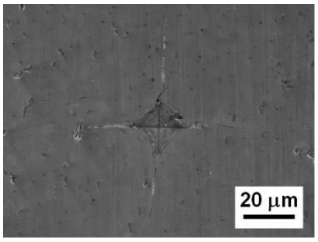

Figure 24. SEM micrograph of Vickers hardness impression in boron carbide made at 1kg indentation load.

Table 3 Young's modulus and hardness values by nanoindentation for 75 impressions

Point #	E, GPa	H, GPa	Point #	E, GPa	H, GPa	Point #	E, GPa	H, GPa
0	373.7	39.2	25	395.5	41.64	50	398.8	40.7
1	302.6	22.6	26	385.4	41.08	51	435.7	46.2
2	380.7	34.2	27	430	41.68	52	421.2	42.2
3	470.2	28.1	28	389.5	39.34	53	432.2	43.9
4	404.4	42.5	29	380.6	36.38	54	464.9	49.4
5	675.5	44.8	30	395.8	42.51	55	431.1	44.1
6	420.9	39.0	31	422.7	45.3	56	423.2	43.2
7	437.6	43.8	32	302	20.79	57	426.8	41.9
8	338.2	23.2	33	405.2	45.37	58	432.9	44.4
9	483.9	38.4	34	381.3	37.47	59	425.2	44.6
10	429.7	34.0	35	389.8	41.68	60	379.3	42.7
11	444.1	42.4	36	403	41.51	61	447.6	42.7
12	415.0	43.3	37	399.6	40.66	62	465.6	47.9
13	428.6	42.7	38	415.6	38.73	63	443.7	45.3
14	480.5	36.9	39	415.8	43.16	64	450.1	46.1
15	408.2	42.4	40	392.7	37.56	65	425.9	43.8
16	421.9	43.4	41	427.3	44.13	66	444.1	45.2
17	358.4	28.5	42	380.8	39.09	67	436	44.9
18	446.6	45.3	43	-	-	68	446.5	45.4
19	416.7	43.7	44	418.5	44.21	69	434.1	41.9
20	421.9	41.7	45	427.3	44.49	70	438.1	42.5
21	434.0	41.5	46	404.8	42.51	71	444.7	45.5
22	453.4	47.2	47	298.8	29.72	72	428.5	41.9
23	447.0	46.8	48	370.1	35.81	73	443.9	46.1
24	435.0	40.9	49	398.3	38.23	74	444.7	44.3

The three different load-displacement plots in Figure 25 illustrate the different types of nanoindentation behavior observed. While many of the measured load-displacement plots were smooth and showed no deviation from a continuous increase in load and displacement (Figure 25A), many of the load-displacement plots showed multiple or at least one pop-in events upon loading (Figure 25C). While only three load-displacement plots in the data set of 50 indentation plots that showed a well pronounced "elbow" effect upon unloading (Figure 25E). The absence or presence of "pop-ins" or "elbows" in the load-displacement plots during loading and unloading of B_4C are indicative of the absence or presence of structural changes such as crystal phase transitions or amorphization. It is generally accepted that the absence of sudden volumetric changes associated with a structural transformation in the material produce a monotonic loading/unloading response during nanoindentation (Figure 25A) [150].

The maximum mean contact pressure under such conditions is about 43 GPa (Figure 25B), which corresponds very well to the average hardness values of 41.1 ± 5.7 GPa (Table 4). Some of the load-displacement plots obtained during nanoindentation of B_4C exhibited one to three discontinuities during loading (Figure 25C). The presence of such pop-in events during nanoindentation is explained by transition from the elastic to elastoplastic deformation upon nano contact in the imprint [111]. A second order phase transition in B_4C was reported to occur at 32 GPa to 35 GPa due to reordering of polar atoms [83]. It was found that this second order transition, which is characterized by atomic site exchange with hysteresis, is a relaxation process that is reversible [85]. It was also predicted that both the chain bending of the three-atom carbon chain and disordering of the structure were detected above 70 GPa, where non-hydrostatic stresses are present.

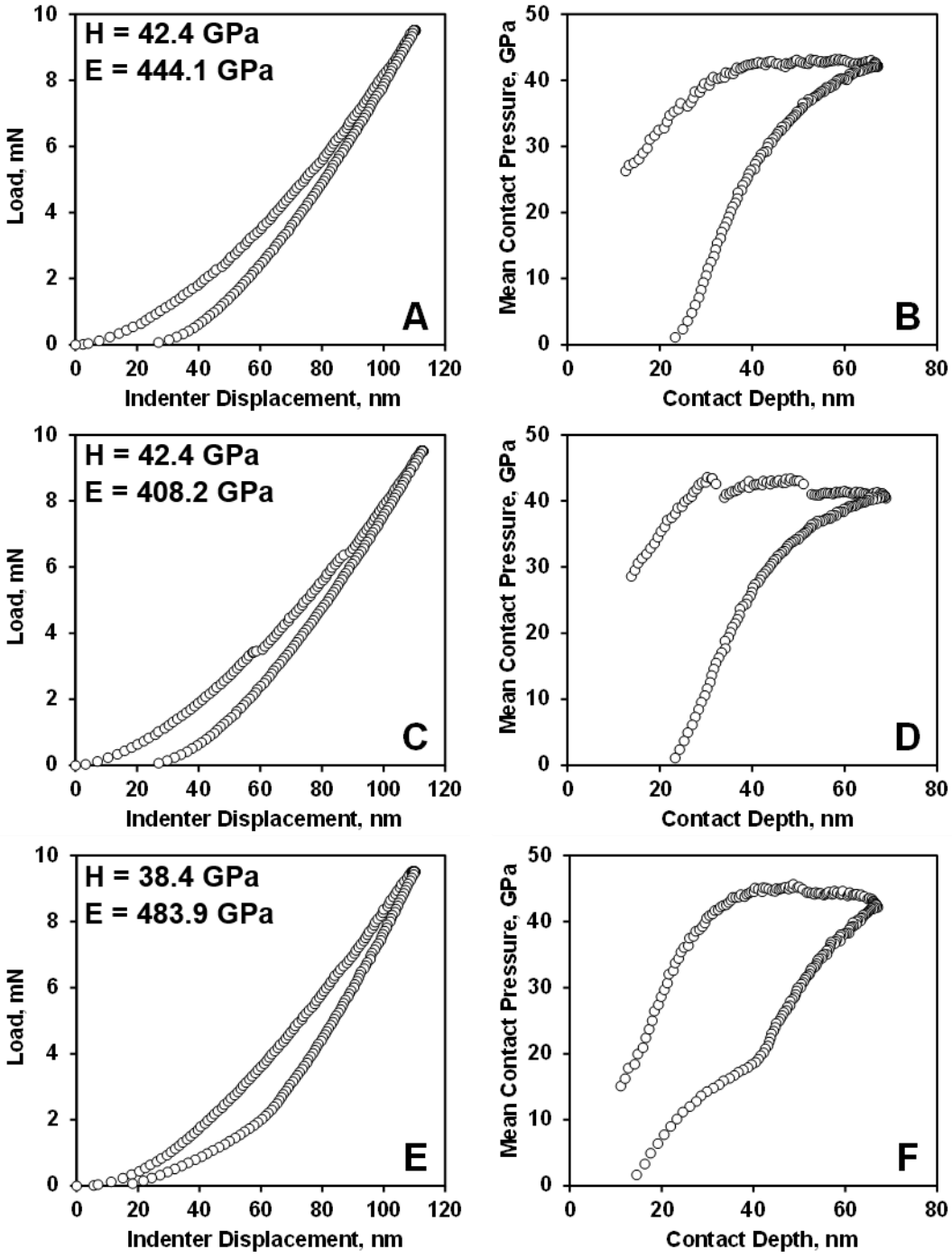

Figure 25. Nanoindentation load-displacement curves for B_4C for loading and unloading with different indentation behavior as well as mean contact pressure.

It was explained that the non-ideal structure of B_4C can activate chain bending guided by polar carbon atom location in the icosahedron even at lower stresses above 38 GPa as observed in shock-wave experiments [151]. The discontinuities during nanoindentation of B_4C occurred first at 43 GPa with a mean contact pressure decreasing to below 40 GPa during this first pop-in event occurring at a contact depth of 20nm (Figure 25D). Upon further loading, the mean contact pressure recovered back to above 40 GPa, where a second pop-in event was detected at a contact penetration depth of about 50nm. The appearance of such pop-in events during loading of B_4C can possibly be explained either by plastic deformation by nucleation of dislocations [111] or a high pressure structural phase transition, with an associated decrease in the volume of the high-pressure phase [83], [151]. The simulated estimate of ~ 4% sudden volume reduction were reported in [152], however, the pressure where such a significant volume change would occur was estimated to be ~ 22.8 GPa. Structural recovery and formation of disordered phases were reported to occur in a number of materials upon unloading [153]. The discontinuities and changes in the slopes upon unloading of B_4C were reported in [104]. In our nanoindentation experiments, three load-displacement nanoindentation plots exhibited the formation of an "elbow" (Figure 25E), which can be explained by the amorphization of the deformed B_4C structure upon unloading and the formation of a phase with larger volume, causing a change in the slope of the mean contact pressure vs contact depth deformation plot (Figure 25F).

Strength and Fracture Toughness of B_4C

While B_4C exhibits a very high Young's modulus and hardness compared to other ceramics, its average flexural strength is not so highs, and it averages between 250-450 MPa [19], [154], [114],

[155], [112], [21], [2], [118]. The flexural strength of B_4C measured in the current research had an average value of 585±70 MPa. The relatively high flexural strength in the current study suggests that the strength determining defects must have been relatively small. A typical stress vs time plot of loading of B_4C in 4-point bending is shown in Figure 26, with inserts showing the fracture surface of B_4C samples after failure.

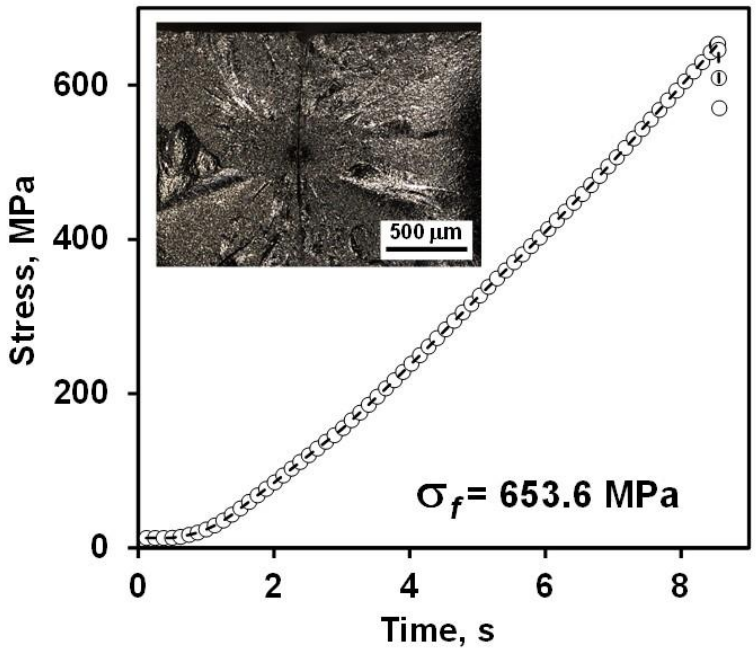

Figure 26. Stress vs time loading plot of B_4C for flexure strength measurements. The insert shows an optical micrographs of fracture surface of B_4C after failure.

The average biaxial strength σ_b of B_4C was measured to be 239±122MPa using a ring-on-ring configuration [133]. The typical stress-strain deformation behavior of B_4C during ring-on-ring loading is shown in Figure 27. The two inserts show micrographs of B_4C samples after failure. As expected, the samples that failed at relatively high loads were broken into multiple pieces after

failure, while the samples that failed at low loads were broken into two pieces, as can be seen in the inserts Figure 27. It is not clear why the strength of B_4C measured in 4-point bending and ring-on-ring tests were so different, but the quality of the surface after machining likely to contributed to such low biaxial strength values.

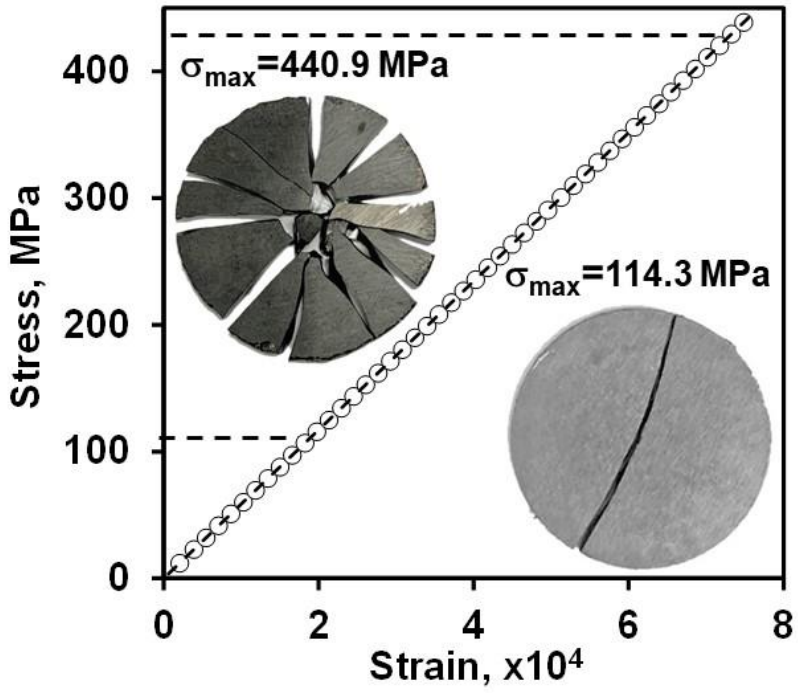

Figure 27. Biaxial stress-strain deformation plot and two photos of B_4C samples that failed at the maximum and the minimum biaxial stress applied.

Weibull modulus m_f is equal to 9.9 for 4-point bending strength values, but the Weibull modulus m_b is only 2.2 for the ring-on-ring strength values (Figure 28). The Weibull distribution for biaxial as well as 4-point bending is presented in the Figure 28. The characteristic strength σ_{0f} was equal to 611 MPa in 4-point bending experiments and the scale parameter σ_{0b} was equal to 271 MPa in ring-on-ring tests (Figure 28).

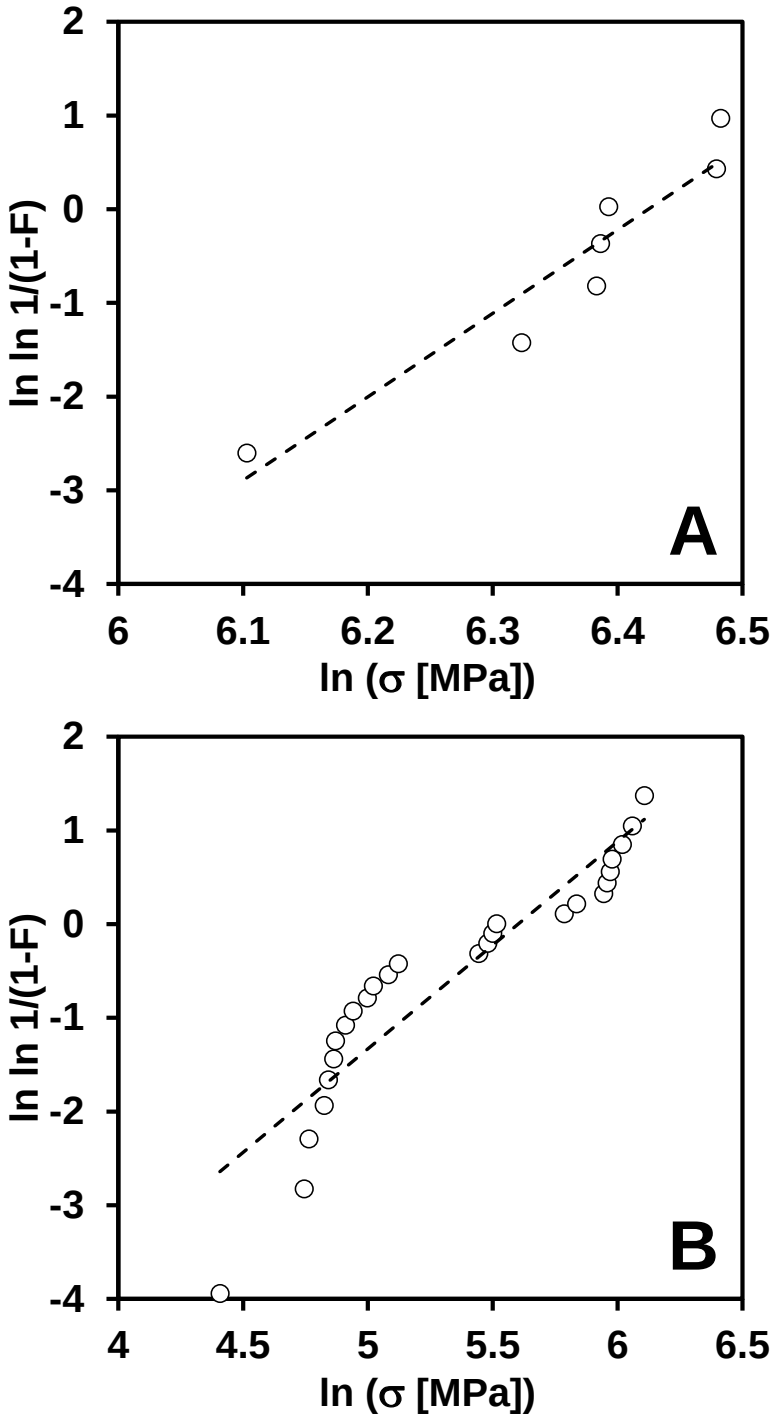

Figure 28. The Weibull probability plots of (A) 4-point flexure strength and (B) ring-on-ring biaxial strength.

The maximum biaxial strength during the mechanical testing of B_4C specimens came out to be 440 MPa with a maximum applied load of 1530N, which was used for a numerical simulation. The stress distribution during biaxial ring-on-ring loading of B_4C was modeled using Abaqus [133], which showed that the highest tensile biaxial strength occurred along the bottom surface of B_4C specimen (Figure 29) and was equal to 436.1 MPa.

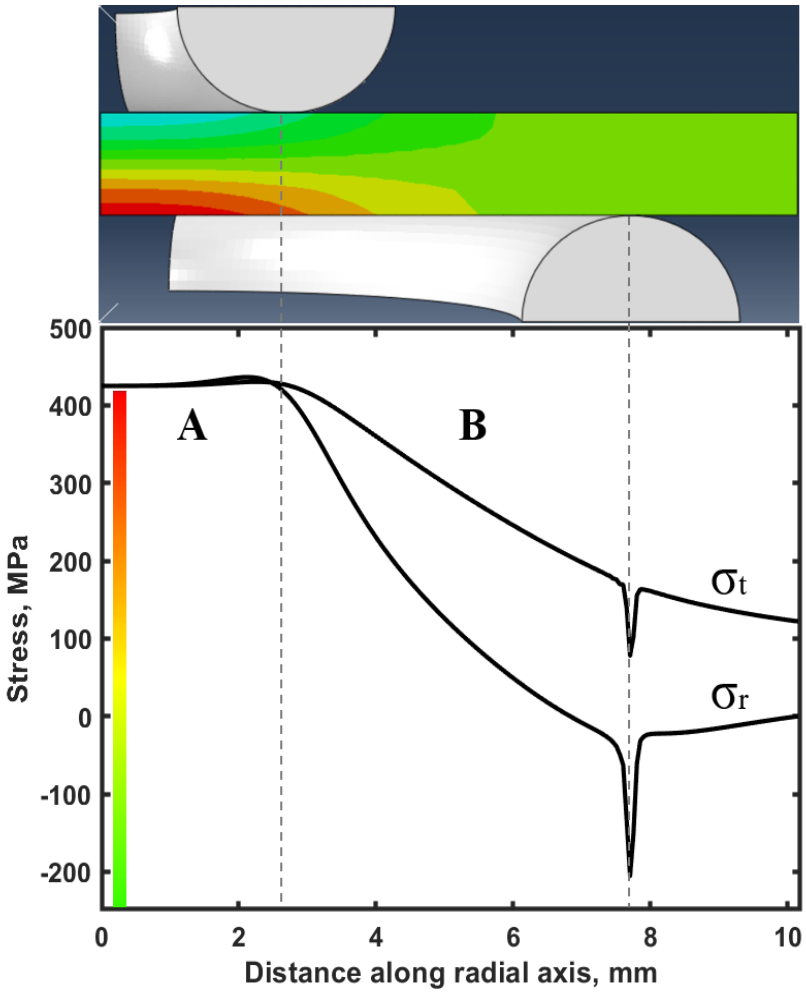

Figure 29. The stress distribution in a B_4C disk upon biaxial loading. σ_r is the stress distribution in the radial direction and σ_t is the stress distribution in the tangential direction.

The region A in Figure 29 represents the highest uniform tensile stresses at the polished bottom surface of B_4C between the surface contact of the specimen and support-ring, as well as a high compressive strength which developed at the line of the contact of the B_4C samples with the load-ring. The region B in the Figure 29 depicts the stresses that are no longer uniform and by the end of region B, at the point when the sample has a contact with the support ring, the compressive stresses rise rapidly, however, it does not represent the critical condition and the values show that it is not a critical point of failure during testing. The stress distribution depicted by a numerical model are similar to those reported in a previous study of the biaxial strength of ZrB_2- SiB_6 ceramic composite [133]. The fracture toughness of B_4C measured by SEVNB was equal to the 3±0.19 MPa $m^{1/2}$. The load vs time plot used for the calculation of K_{Ic} is shown in Figure 30, while the insert shows an optical micrograph of the V-notch with the measured tip diameter equal to 2.1 µm.

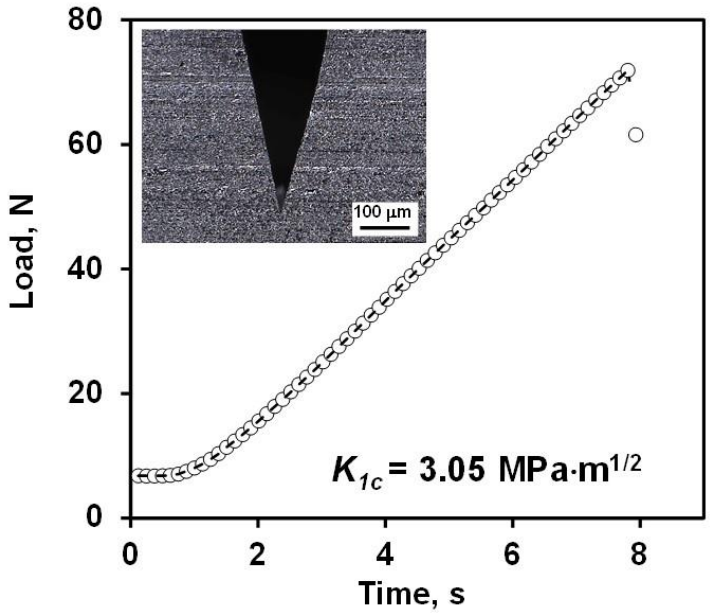

Figure 30. Load vs time plot of B_4C V notched bar used for the calculation of fracture toughness. The insert is an optical micrograph of the V notch.

The collection of all properties and parameters of B_4C measured in this research work is presented in Table 4.

Table 4. Thermal, electrical and mechanical properties of B_4C at room temperature

CTE 10^{-6} K^{-1} (Dilatometer)	6
Ω, Om m	$2.84 \pm 0.9 \cdot 10^{-3}$
E, GPa (IE)	442±3
E, GPa (RUS)	458.7
G, GPa (RUS)	195.7
K, GPa (RUS)	233.3
ν (RUS)	0.173
E, GPa (Nanoindentation)	419.2 ± 47.3
H, GPa (Nanoindentation)	41.1 ± 5.7
H_V, GPa (Vickers)	28.5±1.2
σ_f, MPa (Flexure)	585±70
m_f (Flexure)	9.9
σ_{0f}, MPa (Flexure)	611
σ_b, MPa (Biaxial)	238.6±122
m_b (Biaxial)	2.2
σ_{0b}, MPa (Biaxial)	271
K_{1c}, MPa $m^{1/2}$(SEVNB)	3±0.19

Conclusions

The thermal, electrical and mechanical properties of dense B_4C ceramics (99%) sintered using Spark Plasma Sintering were investigated. It was determined by XRD and Raman spectroscopy that the major phase was indeed B_4C. A minor presence of a C phase was also detected by X-ray diffraction. The grain size of B_4C after sintering was in the range of 2.5-3.5 micron as estimated by SEM. Both the measured thermal expansion and electrical resistivity of the B_4C ceramics is similar to data published in the literature. The Young's modulus of B_4C measured by three different techniques – IE, RUS, and nanoindentation showed a very good overlap in values, which ranges from 419.2 ± 47.3 GPa for nanoindentation to 458.7 GPa for RUS measurements at room

temperature. Both the Young's, shear and bulk moduli decreased by about ~ 5% at 1000 ˚C compared to their room temperature values, however, the Poisson's ratio remained constant at 0.172 in the whole RT to 1000 ˚C temperature range measured by RUS. The difference in hardness values measured by nanoindentation as 41.1 ± 5.7 GPa and Vickers microhardness at 1kg as 28.5±1.2 GPa was expected and it could be explained by indentation size effect and/or formation of radial cracks from the corner of impressions, which relieved the indentation stress and decreased the hardness value above a certain critical load during indentation. The mean contact pressure-contact depth plots obtained from load-displacement nanoindentation data indicated pop-in events during loading and an "elbow" event during unloading, both of which are indicative of possible structural changes in B_4C structure during nanoindentation. The appearance of "elbow" deviations in load-displacement nanoindentation curves of B_4C was detected for the first time. The 4-point bending strength of the B_4C ceramics was o 585±70 MPa with a shape parameter m_f equal to 9.9 and scale parameter σ_{of} equal to 611 MPa. The biaxial strength of B_4C was measured to be much lower and equal to 238.6±122 MPa with a shape parameter of 2.2 and scale parameter σ_{ob} equal to 271 MPa. To the best of our knowledge the biaxial strength of B_4C was also measured for the first time. It was determined that failure of B_4C occurred by fully transgranular fracture, with no intergranular failure. Using the SEVNB technique, a K_{Ic} = 3±0.19 was measured for B_4C, which is similar to previously reported values.

LIST OF REFERENCES

[1] T. Lundstrom, "Structure, defects and properties of some refractory borides," *Pure and Applied Chemistry,* vol. 57, no. 10, p. 1383–1390, 1985.

[2] T. Abzianidze, A. Eristavi and S. Shalamberidze, "Strength and creep in boron carbide (B4C) and aluminum dodecaboride (α-AlB12)," *Journal of Solid State Chemistry,* vol. 154, no. 1, pp. 191-193, 2000.

[3] G. Gogotsi, Y. Groushevsky, O. Dashevskaya, Y. Gogotsi and V. Lavrenko, "Complex investigation of hot-pressed boron carbide," *Journal of the Less Common Metals,* vol. 117, no. 1-2, pp. 225-230, 1986.

[4] V. Dominich , S. Reynaud, R. Haber and M. Chhowalla, "Boron carbide: structure, properties, and stability under stress," *Journal of American Ceramic Society,* vol. 94, no. 11, pp. 3605-3628, 2011.

[5] N. Wiberg, A. Holleman and E. Wiberg, Inorganic Chemistry, San Diego, CA: Academic Press, 2001.

[6] N. Greenwood and A. Earnshaw, Chemistry of the Elements, Burlington, MA: Elsevier Butterworth–Heinemann, 1997.

[7] Y. Gogotsi and R. Andrievski, Materials Science of Carbides, Nitrides and Borides (NATO Science Partnership Sub-Series: 3), St. Petersburg, Russia: Kluwer Academic Publishers, 1999.

[8] I. Higashi, "Crystal Chemistry of α-AlB12 and γ-AlB12," *Journal of Solid State Chemistry,* vol. 154, no. 1, pp. 168-176, 2000.

[9] J. Nagamatsu, N. Nakagawa, T. Muranaka, Y. Zenitani and J. Akimitsu, "Superconductivity at 39 K in magnesium diboride," *Nature,* vol. 410, pp. 63-64, 2001.

[10] M. Tomsic, M. Rindfleisch, J. Yue, K. McFadden, J. Phillips, M. Sumption, M. Bhatia, S. Bohnenstiehl and E. Collings, "Overview of MgB2 superconductor applications," *International Journal of Applied Ceramic Technology,* vol. 4, no. 3, pp. 250-259, 2007.

[11] C. Buzea and T. Yamashita, "Review of the superconducting properties of MgB2," *Supercond. Sci. Technol.,* vol. 14, pp. 115-146, 2001.

[12] K. Vinod, R. Abhilash Kumar and U. Syamaprasad, "Prospects for MgB2 superconductors for magnet application," *Superconductor Science and Technology,* vol. 20, no. 1, 2006.

[13] B. Basu, G. Raju and A. Suri, "Processing and properties of monolithic TiB2 based materials," *International Materials Reviews,* vol. 51, no. 6, pp. 352-374, 2006.

[14] M. Barger, M. Larsson and S. Hogmark, "Evaluation of magnetron-sputtered TiB2 intended for tribological applications," *Surface and Coatings Technology*, vol. 124, no. 2-3, pp. 253-261, 2000.

[15] S. Suresh, N. Shenbag and V. Moorthi, "Aluminium-titanium diboride (Al-TiB2) Metal Matrix Composites: Challenges and Opportunities," *Procedia Engineering*, vol. 38, pp. 89-97, 2012.

[16] X. Wang, R. Brydson and J. Ellis, "Microstructural analysis of Al alloys dispersed with TiB2 particulate for MMC applications," *Journal of Microscopy*, vol. 196, no. 2, pp. 137-145, 1999.

[17] S. Shu, H. Yang, C. Tong and F. Qiu, "Fabrication of TiCx-TiB2/Al Composites for Application as a Heat Sink," *Materials*, vol. 9, no. 642, 2016.

[18] F. Monteverde and R. Savino, "ZrB2–SiC Sharp leading edges in high enthalpy supersonic flows," *The American Ceramic Society*, vol. 95, no. 7, pp. 2282-2289, 2012.

[19] F. Thevenot , "Boron carbide—a comprehensive review," *Journal of the European Ceramic Society*, vol. 6, pp. 205-225, 1990.

[20] B. Matchen, "Applications of ceramics in armor products," *Key Engineering Materials* , Vols. 122-124, pp. 333-344, 1996.

[21] A. Lipp, "Boron carbide: production properties, aplications," *Tech. Rundsch*, vol. 58, no. 7, pp. 1-47, 1966.

[22] J. van der Laan, G. Schnedecker, E. van Osch, R. Duwe and J. Linke, "Plasma-sprayed boron carbide coatings for first-wall protection," *Journal of Nuclear Materials*, vol. 211, no. 2, pp. 135-140, 1994.

[23] R. Jimbou, M. Saidoh, K. Nakamura, M. Akiba, S. Suzuki, Y. Gotoh, Y. Suzuki, A. Chiba, T. Yamaki, M. Nakagawa, K. Morita and B. Tsuchiya, "New composite composed of boron carbide and carbon fiber with high thermal conductivity for first wall," *Journal of Nuclear Materials* , Vols. 233-237, pp. 781-786, 1996.

[24] O. de Luze, "Degradation and oxidation of B4C control rod segments at high temperatures. A review and code interpretation of the BECARRE program," *Nuclear Engineering and Design* , vol. 259, pp. 150-165, 2013.

[25] P. Valentine, P. Trester, J. Winter, J. Linke, R. Duwe, E. Wallura and V. Philipps, "Boron carbide based coatings on graphite for plasma-facing components," *Journal of Nuclear Materials*, Vols. 212-215, no. Part B, pp. 1146-1152, 1994.

[26] C. Homann, W. Hering and G. Schanz, "Analysis and comparison of experimental data of bundle tests QUENCH-07 to QUENCH-09 about B4C control rod behaviour," FZKA 7107, Karlsruhe, 2006.

[27] M. Mortensen, P. Sorensen, O. Bjorkdahl, M. Jensen, H. Gundersen and T. Bjornholm, "Preparation and characterization of boron carbide nanoparticles for use as a novel agent in T cell-guided boron neutron capture thera," *Applied Radiation and Isotopes,* vol. 64, no. 3, pp. 315-324, 2006.

[28] A. Bellosi, S. Guicciardi, V. Medri, F. Monteverde, D. Sciti and L. Silvestroni, Boron Rich Solids: Sensors, Ultra High Temperature Ceramics, Thermoelectrics, Armor , Processing and Properties of Ultra-Refractory Composites Based on Zr- and Hf-Borides: State of the Art and Perspectives, 2010.

[29] K. Morsi and V. Patel, "Processing and properties of titanium–titanium boride (TiBw) matrix composites—a review," *Journal of Materials Science,* vol. 42, pp. 2037-2047, 2007.

[30] M. Bougoin and F. Thevenot, "Pressureless sintering of boron carbide with an addition of polycarbosilane," *Journal of Materials Science,* vol. 22, no. 1, pp. 109-114, 1987.

[31] A. Chamberlain, W. Fahrenholtz and G. Hilmas, "Pressureless sintering of zirconium diboride," *Journal of the American Ceramic Society ,* vol. 89, no. 2, pp. 450-456, 2005.

[32] "Opportunities in protective materials science and technology for future army applications," *National Research Council of the National Academies,* pp. 69-98, 2011.

[33] X. Wang, W. Guo and G. Zhang, "Pressureless sintering mechanism and microstructure of ZrB2–SiC ceramics doped with boron," *Scripta Materialia,* vol. 61, no. 2, pp. 177-180, 2009.

[34] J. Zimmermann, W. Hilmas, W. Fahrenholtz, F. Monteverde and A. Bellosi, "Fabrication and properties of reactively hot pressed ZrB2–SiC ceramics," *Journal of the European Ceramic Society,* vol. 27, no. 7, pp. 2729-27-36, 2007.

[35] P. Boch, J. Glandus, L. J. Jarrige and J. Mexmain, "Sintering, oxidation and mechanical properties of hot pressed aluminium nitride," *Ceramics International,* vol. 8, no. 1, pp. 34-40, 1982.

[36] R. German, Sintering: From Empirical Observations to Scientific Principles, Butterworth-Heinemann, 2014.

[37] H. Atkinson and S. Davies, "Fundamental aspects of hot isostatic pressing: An overview," *Metallurgical and Materials Transactions A ,* vol. 31, pp. 2981-3000, 2000.

[38] F. Swinkels, D. Wilkinson, E. Arzt and M. Ashby, "Mechanisms of hot-isostatic pressing," *Acta metallurgica,* pp. 1829-1840, 1983.

[39] A. Muley, S. Aravindan and I. Singh, "Nano and hybrid aluminum based metal matrix composites: An overview," *Manufacturing Rev.,* vol. 2, no. 15, 2015.

[40] H. Wang, S. Lee, H. Kim and H. Oh, "Synthesis of ultrafine hafnium diboride powders using solution-based processing and spark plasma sintering," *International Jouran of Applied Ceramic Technology*, vol. 11, no. 2, pp. 359-363, 2013.

[41] E. Olevsky and L. Froyen, "Impact of thermal diffusion on densification during SPS," *J. of the Am. Ceram. Soc.*, vol. 92, no. S1, pp. 122-132, 2009.

[42] F. Monteverde, "Ultra-high temperature HfB2–SiC ceramics consolidated by hot-pressing and spark plasma sintering," *Journal of Alloys and Compounds*, vol. 428, pp. 197-205, 2007.

[43] Z. Shen, M. Johnsson, Z. Zhao and M. Nygren, "Spark plasma sintering of alumina," *Journal of the American Ceramic Society* , vol. 85, no. 8, pp. 1921-1927, 2002.

[44] O. Guillon, J. Gonzalez-Julian, B. Dargatz, T. Kessel, G. Schierning, J. Rathel and M. Herrmann, "Field-Assisted Sintering Technology/Spark Plasma Sintering: Mechanics, Materials, and Technology Developements," *Journal of Advanced Engineering Materials*, vol. 16, no. 7, pp. 830-849, 2014.

[45] S. Grasso, T. Graves Saunders, R. McKinnon, E. Castle, P. Tatarko, B. Du, Y. M. Gucci, H. Porwal, B. Milson and M. Reece, "Spark plasma sintering in a flash," *American Ceramic Society Bulletin*, vol. 95, no. 7, pp. 32-34, 2016.

[46] M. Cologna, B. Rashkiva and R. Raj, "Flash sintering of nanograin zirconia in <5 s at 850°C," *Journal of the American Ceramic Society* , vol. 93, no. 11, pp. 3556-3559, 2010.

[47] S. Grasso, T. Saunders, H. Porwal, O. Cedillos-Barraza, D. Doni Jayaseelan, W. Lee and M. Reece, "Flash Spark Plasma Sintering (FSPS) of pure ZrB2," *Journal of the American Ceramic Society* , vol. 97, no. 8, pp. 2405-2408, 2014.

[48] E. Olevsky, S. Rolfing and A. Maximenko, "Flash (Ultra-Rapid) spark-plasma sintering of silicon carbide," *Scientific Reports* , vol. 6, no. 33408, 2016.

[49] C. Maniere, G. Lee and E. Olevsky, "All-materials-Inclusive flash spark plasma sintering," *Scientific Reports*, vol. 7, no. 1, 2017.

[50] M. Bouchacourt and F. Thevenot, "The properties and structure of the boron carbide phase," *Jpurnal of the Less Common Metals*, vol. 82, pp. 227-235, 1981.

[51] R. Lazzari, N. Vast, J. Besson, S. Baroni and A. Dal Corso, "Atomic structure and vibrational properties of icosahedral B4C boron carbide," *Physical Review Letters*, vol. 83, no. 16, pp. 3230-3233, 1999.

[52] N. Hosmane, J. Maguire and Z. Yinghuai, "Polyhedral boron cage compounds: an account," *Journal Main Group Chemistry* , vol. 5, no. 4, pp. 251-265, 2007.

[53] G. Zhdanov and N. Sevastyanov, "Crystal structure of boron carbide (B4C)," *Doklady Akademii Nauk SSSR,* vol. 32, 1941.

[54] T. Aselage and R. Tissot, "Lattice constants of boron carbides," *Journal of the American Ceramic Society,* vol. 75, no. 8, pp. 2207-2212, 1992.

[55] G. Kwei and B. Morosin, "Structures of the boron-rich boron carbides from neutron powder diffraction: implications for the nature of the inter-icosahedral chains," *The Journal of Physical Chemistry ,* vol. 100, no. 19, pp. 8031-8039, 1996.

[56] T. Aselage and R. Tissot, "Lattice constants of boron carbides," *Journal of the American Ceramic Society,* vol. 75, no. 8, pp. 2207-2212, 1992.

[57] X. Guo, J. He, Z. Liu, Y. Tian, J. Sun and H. Wang, "Bond iconicity and hardness of B13C2-like structured ByX crystals (X, C, N, O, P, As)," *Phys. Rev. B,* vol. 73, no. 10, pp. 104-115, 2006.

[58] A. Kirfel, A. Gupta and G. Will, "The nature of the chemical bonding in boron carbide, B13C2. I. Structure refinement," *Acta Cryst.,* vol. B, no. 35, pp. 1052-1059, 1979.

[59] H. Yakel, "The crystal structure of boron-rich boron carbide," *Acta Cryst.,* vol. B, no. 31, pp. 1797-1806, 1975.

[60] G. Tsagareishvili, "Thermal expansion of boron and boron carbide," *J. Less Common Met.,* vol. 117, pp. 159-161, 1986.

[61] R. Telle, "Boride----eine neue Hartstoffgeneration," *Chemic unserer Zeit,,* vol. 22, pp. 93-99, 1988.

[62] G. Hollenberg, "Thermally induced stresses and fractures in boron carbide pellets," *Ceram. Bull,* vol. 59, pp. 538-541, 1980.

[63] J. Lagrenaudie, "A study of the properties of boron," *J. Phys.-Paris,* vol. 14, pp. 14-18, 1953.

[64] H. Werheit, "On excitons and other gap states in boron carbide," *J. Phys. Condens. Mat.,* vol. 18, no. 47, pp. 10655-10662, 2006.

[65] H. Werheit, "Systematic error in conventionally measured Raman spectra of boron carbide—A general issue in solid state Raman spectroscopy," *Review of Scientific Instruments 90, 043114,* 2019.

[66] C. Wood and D. Emin, "Conduction mechanism in boron carbide," *Phys. Rev. B,* vol. 31, no. 10, pp. 6811-6814, 1985.

[67] L. Zuppiroli, N. Papandreou and R. Kormann, "The dielectric response of boron-carbide due to hopping conduction," *J. Appl. Phys.,* vol. 70, no. 1, pp. 246-252, 1991.

[68] R. Schmechel and H. Werheit, "Evidence of the superposition of drude type and hopping type transport in boron-rich solids," *J. Solid State Chem.,* vol. 133, no. 1, pp. 335-341, 1997.

[69] K. Shirai and S. Emura, "Lattice vibrations and the bonding nature of boron carbide," *Journal of Physics: Condensed Matter,* vol. 8, no. 50, pp. 10919-10929, 1996.

[70] M. Chen , J. McCauley and K. Hemker, "Shock-induced localized amorphization in boron carbide," *Science,* vol. 299, pp. 1563-1566, 2003.

[71] T. Vogler, W. Reinhart and L. Chhabildas, "Dynamic behavior of boron carbide," *Appl. Phys.,* vol. 95, no. 8, pp. 4173-4183, 2004.

[72] M. Wilkins, "Third progress report of light armor program," Lawrence Livermore National Laboratory, University of California, CA, 1968.

[73] R. McQueen, S. Marsh, J. Taylor, J. Frotz and W. Carter, "The equation of state of solids from shock wave studies," in *High-Velocity Wave Phenomena*, New York, Academic Press, 1970, pp. 239-417.

[74] M. Pavlovskii, "Shock compressibility of six very hard substances," *Sov. Phys. Solid State,* vol. 12, pp. 1736-1737, 1971.

[75] W. Gust and E. Royce, "Dynamic yield strengths of B4C, BeO, and Al2O3 ceramics," *Appl. Phys.,* vol. 42, no. 1, pp. 276-295, 1971.

[76] D. Grady, "Shock-wave strength properties of boron carbide and silicon carbide," *J. Phys. IV,* vol. 4, pp. 385-391, 1994.

[77] V. Dominich and Y. Gogotsi, "Nanoindentation and Raman spectroscopy studies of boron carbide single crystals," *Appl. Phys. Lett.,* vol. 81, p. 3783, 2002.

[78] X. Yan, W. Lo, T. Goto and M. Chen, "Raman spectroscopy of pressure-induced amorphous boron carbide," *Appl. Phys. Lett.,* vol. 88, no. 131905, 2006.

[79] D. Ge, V. Dominich, T. Juliano, E. Stach and Y. Gogotsi, "Structural damage in boron carbide under contact loading," *Acta Mater.,* vol. 52, no. 13, pp. 3921-3927, 2004.

[80] D. Ghosh, G. Subhash, C. Lee and Y. Yap, "Strain-induced formation of carbon and boron clusters in boron carbide during dynamic indentation," *Appl. Phys. Lett.,* vol. 91, no. 6, 2007.

[81] D. Ghosh, G. Subhash, T. Sudarshan, R. Radhakrishnan and X. Gao, "Dynamic indentation response of fine-grained boron carbide," *J. Am. Ceram. Soc.,* vol. 90, no. 6, pp. 1850-1857, 2007.

[82] M. Chen and J. McCauley, "Mechanical scratching induced phase transitions and reactions of boron carbide," *J. Appl. Phys.,* vol. 100, no. 123517, 2006.

[83] H. Werheit, M. Manghnani and A. Hushur, "Phonon peculiarities at the high-pressure phase transition of B4.3C boron carbide," *Solid State Sciences,* vol. 97, no. 105978, 2019.

[84] H. Werheit, "Assignment of the electronic transitions in B4.3C boron carbide implies a specifically distorted crystal structure," *Solid State Sciences,* vol. 86, pp. 38-44, 2018.

[85] H. Werheit, M. Manghnani, U. Kuhlmann, A. Hushur and S. Shalamberidze, "Mode Grüneisen parameters of boron carbide," *Solid State Sciences ,* vol. 72, pp. 80-93, 2017.

[86] A. Hushur, M. Manghnani, H. Werheit, P. Dera and Q. Williams, "High-pressure phase transition makes B4.3C boron carbide a wide-gap semiconductor," *Journal of Physics: Condensed Matter,* vol. 28, no. 4, 2016.

[87] P. Dera, M. Manghnani, A. Hushur, Y. Hu and S. Tkachev, "New insights into the enigma of boron carbide inverse molecular behavior," *Journal of Solid State Chemistry,* vol. 215, pp. 85-93, 2014.

[88] S. Lee, D. Bylander and L. Kleinman, "Elastic moduli of B-12 and its compounds," *Phys. Rev.,* vol. 45, no. 7, pp. 3245-3247, 1992.

[89] K. McClellan, F. Chu, J. Roper and I. Shindo, "Room temperature single crystal elastic constants of boron carbide," *Journal of Materials Science,* vol. 36, no. 14, pp. 3403-3407, 2001.

[90] S. Dodd, G. Saunders and B. James, "Temperature and pressure dependences of the elastic properties of ceramic boron carbide (B4C)," *JOURNAL OF MATERIALS SCIENCE,* vol. 37, pp. 2731-2736, 2002.

[91] W. Gust and E. Royce, "Dynamic yield strengths of B4C, BeO, and Al2O3 ceramics," *Journal of Applied Physics,* vol. 42, no. 276, 1971.

[92] T. Asselage, D. Tallant, J. Gieske, S. Van Deusen and R. Tissot, "The physics and chemistry of carbides; nitrides and borides," *Kluwer Academic Publishers,* p. 97, 1990.

[93] J. Gieske, T. Aselage and D. Emin, "Boron rich solids," in *AIP Conf. Proc. No. 231,* New York, 1991.

[94] G. De With, "High temperature fracture of boron carbide: experiments and simple theoretical models," *Journal of Materials Science,* vol. 19, pp. 457-466, 1984.

[95] G. Gogotsi, S. Firstov, A. Vasil'ev, Y. Gogotsi and V. Kovylyaev, "Mechanical properties and special features of the structure of materials based on boron carbide," *Soviet Powder Metallurgy and Metal Ceramics,* vol. 26, no. 7, pp. 589-594, 1987.

[96] K. Sairam, J. Sonber, T. Murthy, C. Subramanian, R. Hubli and A. Suri, "Development of B4C–HfB2 composites by reaction hot pressing," *International Journal of Refractory Metals and Hard Materials ,* vol. 35, pp. 32-40, 2012.

[97] M. Manghnani, Y. Wang, P. Zinin and W. Rafaniello, "Elastic and vibrational properties of B4C to 21 GPa," *Science and Technology of High Pressure,* pp. 945-948, 2000.

[98] K. Schwetz and W. Grellner, "The influence of carbon on the microstructure and mechanical properties of sintered boron carbide," *Journal of the Less Common Metals,* vol. 82, pp. 37-47, 1981.

[99] S. Murthy, "Elastic properties of boron carbide," *J. Mater. Sci. Lett.,* vol. 4, no. 5, pp. 603-605, 1985.

[100] J. Gieske, T. Aselage and D. Emin, "Elastic properties of boron carbides," *Boron-Rich Solids. AIP Conf. Proc.,* vol. 231, pp. 376-379, 1991.

[101] R. Nelmes, J. Loveday, R. Wilson, W. Marshal, J. Besson, S. Klotz, G. Hamel, T. Aselage and S. Hull, "Observation of inverted-molecular compression in boron carbide," *Phys. Rev. Lett.,* vol. 74, no. 12, pp. 2268-2271, 1995.

[102] S. Aydin and M. Simsek, "Hypothetically superhard boron carbide structures with a B11C icosahedron and three-atom chain," *Phys. Status Solidi B,* vol. 246, no. 1, pp. 62-70, 2009.

[103] B. Moshtaghioun, F. Cumbrera-Hernandes, D. Gomez-Garcia, A. Dominiguez-Rodriguez, A. Monshi and M. Abbasi, "Effect of spark plasma sintering parameters on microstructure and room-temperature hardness and toughness of fine-grained boron carbide (B4C)," *Journal of the European Ceramic Society,* vol. 33, no. 2, pp. 361-369, 2013.

[104] B. Moshtaghioun, M. Laguna-Bercero, D. Gomez-Garcia and J. Pena, "Does grain size have an influence on intrinsic mechanical properties and conduction mechanism of near fully-dense boron carbide ceramics?," *Journal of Alloys and Compounds,* vol. 795, pp. 408-415, 2019.

[105] M. Devries, J. Pittari, G. Subash, K. Mills, C. Haines and J. Zheng, "Rate-dependent mechanical behavior and amorphization of ultrafine-grained boron carbide," *Journal of the American Ceramic Society,* vol. 99, no. 10, pp. 3398-3405, 2016.

[106] H. Lee and R. Speyer, "Hardness and fracture toughness of pressureless-sintered boron carbide (B4C)," *Journal of the Americal Ceramic Society,* vol. 85, no. 5, pp. 1291-1293, 2002.

[107] R. Kuliiev, N. Orlovskaya, H. Hyer, Y. Sohn, M. Lugovy, D. Ha, M. Radovic, E. Castle, M. Reece, P. Warriam Sasikumar, L. Conti, G. Blugan, T. Graule and J. Kuebler, "Spark plasma sintered B4C: structural, thermal, electrical and mechanical properties," *Materials,* Submitted for publication - 2020.

[108] R. Allen, "The solid solution series boron – boron carbide," *J. Am. Chem. Soc.,* vol. 75, no. 3582, 1953.

[109] M. Bouchacourt and F. Thevenot, "Etudes sur le carbure de bore. I. Métallographie et microdureté Knoop du carbure de bore," *J. Less-Common Met.,* vol. 59, pp. 119-130, 1978.

[110] M. Bougoin, F. Thevenot, F. Dubois and G. Fantozzi, "Synthese et caracterisation de ceramiques denses en carbure de bore," *J. Less Common. Met.*, vol. 114, pp. 257-271, 1985.

[111] S. Dub, V. Kushch, O. Kaidash, V. Sereda and T. Panasyuk, "Initiation of a plastic flow in boron carbide at nanoindentation," *Journal of Superhard Materials,* vol. 37, no. 1, pp. 8-13, 2015.

[112] P. Kisly, M. Kuzenkova, N. Bondarchuk and B. Grabchuk, "Boron Carbide," *Naukova Dumka ,* p. 216, 1988.

[113] J. Swab, C. Meredith, D. Casem and W. Gamble, "Static and dynamic compression strength of hotpressed boron carbide using a dumbbell-shaped," *Journal of Materials Science,* vol. 52, no. 17, pp. 10073-10084, 2017.

[114] S. Hayun, V. Paris, M. Dariel, N. Frage and E. Zaretzky, "Static and dynamic mechanical properties of boron carbide processed by spark plasma sintering," *Journal of the European Ceramic Society,* vol. 29, no. 16, pp. 3395-3400, 2009.

[115] N. Bourne, "Shock–induced brittle failure of boron carbide," *The Royal Society,* vol. 458, no. 2024, 2002.

[116] H. Lee and R. Speyer, "Hardness and fracture toughness of pressureless-sintered boron carbide (B4C)," *Journal of the American Ceramic Society,* vol. 85, no. 5, pp. 1291-1293, 2002.

[117] R. Gettings and D. George, "Surface crack in flexure (SCF) measurements of the fracture toughness of advanced ceramics," *The American Ceramic Society,* vol. 16, 1995.

[118] L. Vargas-Gonzalez, R. Speyer and J. Stephen , "Flexural strength, fracture toughness, and hardness of silicon carbide and boron carbide armor ceramics," *International Journal of Applied Ceramic Technology,* vol. 7, no. 5, pp. 643-651, 2010.

[119] S. Hughes, "Archimedes revisited: a faster, better, cheaper method of accurately measuring the volume of small objects," *Physics Education,* vol. 40, no. 468, 2005.

[120] Determination of Young's modulus, shear modulus and Poisson's ratio, Brussels, Belgium: European Committee for Standardization, 2006.

[121] A. Migliori and J. Sarrao, Resonant Ultrasound Spectroscopy: Applications to Physics,Materials Measurements and Nondestructive Evaluation, New York: John Wiley and Sons, 1997.

[122] M. Radovik, M. Barsoum , A. Ganguly, T. Zhen, P. Finkel, S. Kalidindi and E. Lara-Curzio, "On the elastic properties and mechanical damping of Ti3SiC2, Ti3GeC2, Ti3Si0.5Al0.5C2 and Ti2AlC in the 300–1573 K temperature range," *Acta Materialia*, vol. 54, no. 10, pp. 2757-2767, 2006.

[123] M. Radovic and E. Lara-Curzio, "Mechanical properties of tape cast nickel-based anode materials for solid oxide fuel cells before and after reduction in hydrogen," *Acta Materialia*, vol. 52, no. 20, pp. 5747-5756, 2004.

[124] M. Radovic, E. Lara-Cruzio and L. Riester, "Comparison of different experimental techniques for determination of elastic properties of solids," *Materials Science and Engineering: A*, vol. 368, no. 1-2, pp. 56-70, 2004.

[125] K. McClellan, F. Chu, J. Roper and I. Shindo, "Room temperature single crystal elastic constants of boron carbide," *Journal of Materials Science* , vol. 36, no. 14, pp. 3403-3407, 2001.

[126] W. Oliver and G. Pharr, "An improved technique for determining hardness and elastic modulus using load and displacement sensing indentation experiments," *Journal of Materials research* , vol. 7, no. 3, pp. 613-617, 1992.

[127] G. Pharr, W. Oliver and F. Brotzen , "On the generality of the relationship among contact stiffness, contact area, and elastic modulus during indentation".

[128] N. Novikov, S. Dub, Y. Miladin, I. Gridneva and S. Chugunova, "Application of nanoidentation method to study a semiconductor-metal phase transformation in silicon," *Journal of Superhard Materials (Sverkhtverdye Materialy)*, vol. 18, no. 3, pp. 37-46, 1996.

[129] W. Oliver and G. Pharr, "An improved technique for determining hardness and elastic modulus using load and displacement sensing indentation experiments," *Journal of Materials Research*, vol. 7, no. 6, pp. 1564-1583, 1992.

[130] I. Sneddon, "The relation between load and penetration in the axisymmetric boussinesq problem for a punch of arbitrary profile," *International Journal of Engineering Science*, vol. 3, no. 1, pp. 47-57, 1965.

[131] G. Dieter, Mechanical metallurgy, 3rd edn., Boston, MA: McGraw-Hill Book Company, 1986.

[132] Mechanical Properties of Monolithic Ceramics at Room Temperature – Part 1: Determination of Flexural Strength, Brussles, Belgium: Advanced Technical Ceramics, 2006.

[133] A. Carrasco-Pena, R. Jordan, J. Dieguez, A. Coronado-Rodriguez, V. Ozdemir, K. Kwok, N. Orlovskaya, D. Vazquez-Molina, F. Uribe-Romo, A. Bolon, M. Radovic, S. Grasso and M. Reece, "Design and development of ring-on-ring jig for biaxial strength testing

of brittle ceramic composite materials: ZrB2-30wt-%SiB6," *Advances in Applied Ceramics*, vol. 118, no. 4, pp. 159-168, 2019.

[134] ASTM C1499. Standard Test Method for Monotonic Equibiaxial Flexural Strength of Advanced Ceramics at Ambient Temperature. doi:10.1520/C1499-15, www.astm.org, West Conshohocken, PA, 2003.

[135] M. Mashhadi, E. Taheri-Nassaj, V. Sglavo, H. Sarpoolaky and N. Ehsani, "Effect of Al addition on pressureless sintering of B4C," *Ceramics International* , vol. 35, no. 2, pp. 831-837, 2007.

[136] I. Bogomol, H. Borodianska, T. Zhao, T. Nishimura, Y. Sakka, P. Loboda and O. Vasylkiv, "A dense and tough (B4C–TiB2)–B4C 'composite within a composite' produced by spark plasma sintering," *Scripta Materialia* , vol. 71, no. 15, pp. 17-20, 2014.

[137] W. Weibull, "A statistical distribution function of wide aplicability," *Journal of Applied Mechanics,* vol. 18, pp. 293-297, 1951.

[138] N. Orlovskaya, H. Peterlik, M. Marczewski and K. Kromp, "The validity of Weibull estimators – experimental verification," *Journal of Materials Science,* vol. 32, pp. 1903-1907, 1997.

[139] N. Orlovskaya, H. Peterlik, W. Steinkellner and K. Kromp, "Prediction of strength of recrystallized siliconcarbide from pore size measurement Part I The bimodality of the distribution," *Journal of Materials Science,* vol. 35, no. 3, pp. 699-705, 2000.

[140] H. Peterlik, N. Orlovskaja, W. Steinkellner and K. Kromp, "Prediction of strength of recrystallized siliconcarbide from pore size measurement Part II The reliability of the prediction," *Journal of Materials Science,* vol. 35, no. 3, pp. 707-711, 2000.

[141] "CEN/TS 14425-5, Advanced technical ceramics - test methods for determination of fracture toughness of monolitic ceramics," *Comite Europeen de Normalisation,* 2004.

[142] J. Kubler, Fracture Toughness of Ceramics Using the SEVNB Method: First Results of a Joint VAMAS/ESIS Round Robin, 23rd Annual Conference on Composites, Advanced Ceramics, Materials, and Structures, 2008.

[143] H. Clarck and J. Hoard, "The crystal structure of boron carbide," *Journal of the Americal Chemical Society*, vol. 65, pp. 2115-2119, 1943.

[144] K. Xie, V. Dominich, L. Farbaniec, C. Bin , K. Kuwelkar, L. Ma, J. MvCauley, R. Haber, M. Chen and K. Hemker, "Microstructural characterization of boron-rich boron carbide," *Acta Materialia,* vol. 136, pp. 202-214, 2017.

[145] A. Chennakesava Reddy, "Evaluation of thermal expansion of Al/B4C metal matrix composites," *3rd National Conference on Materials and Manufacturing Processes* , pp. 196-200, 2002.

[146] S. Huang, K. Vanmeensel, O. Malek, O. Van der Biest and J. Vleugels, "Microstructure and mechanical properties of pulsed electric current sintered B4C–TiB2 composites," *Materials Science and Engineering:A,* vol. 528, no. 3, pp. 1302-1309, 2011.

[147] S. Huang, K. Vanmeensel, O. Van der Biest and J. Vleugels, "In situ synthesis and densification of submicrometer-grained B4C–TiB2 composites by pulsed electric current sintering," *Journal of the Europea Ceramic Society* , vol. 31, no. 4, pp. 637-644, 2011.

[148] N. Vast, R. Lazzari, J. Besson, S. Baroni and A. Dal Corso, "Atomic structure and vibrational properties of icosahedral α-boron and B4C boron carbide," *Computational Material Science,* vol. 17, no. 2-4, pp. 127-132, 2000.

[149] S. Dub, V. Brazhkin, V. Belous, G. Tolmacheva and P. Kononevskii, "Comparative nanoindentation of single crystals of hard and superhard oxidess," *Journal of Superhard Materials* , vol. 36, no. 4, pp. 217-230, 2014.

[150] V. Domnich, S. Reynaud, R. Haber and M. Chhowalla, "Boron carbide: structure, properties, and stability under stress," *Journal of the American Ceramic Society,* vol. 94, no. 11, pp. 3605-3628, 2011.

[151] Y. Zhang, T. Mashimo, Y. Uemura , M. Uchino, M. Kodama, K. Shibata, K. Fukuoka, M. Kikuchi, T. Kobayashi and T. Sekine, "Shock compression behaviors of boron carbide (B4C)," *Journal of Applied Physics,* vol. 100, no. 113536, 2006.

[152] X. Yan, Z. Tang, L. Zhang, J. Guo, C. Jin, Y. Zhang, T. Goto, J. McCauley and M. Chen, "Depressurization amorphization of single-crystal boron carbide," *Physical Rev,* vol. 102, no. 075505, 2009.

[153] V. Dominich and Y. Gogotsi, "Indentation induced phase transformation in organics," in *High-Pressure Surface Science and Engineering*, Bristol and Philadelphia, Institute of Physics , 2003, pp. 443-446.

[154] X. Zhang, Z. Zhang, R. Wen, G. Wang, X. Zhang, J. Mu, H. Che and G. Wang, "Comparisons of the densification, microstructure and mechanical properties of boron carbide sintered by hot pressing and spark plasma sintering," *Ceram. Int.* , vol. 44, pp. 2615-2619, 2018.

[155] Q. Song, Z. Zhang, Z. Hu, S. Yin, H. Wang, H. Wang and X. Cheng, "Fully dense B4C ceramics fabricated by spark plasma sintering at relatively low temperature," *Materials Research Express,* vol. 5, no. 10, 2018.

[156] K. Niihara, A. Nakahira and T. Hirai, "The effect of stoichiometry on mechanical properties of boron carbide," *Journal of The American Ceramic Society,* vol. 67, no. 1, pp. C13-14, 1983.

[157] D. Emin, T. Aselage , C. Beckel , A. Switendick and B. Morosin, "Boron-rich solid s(AIP Conf. Proc. 231)," *American Institute of Physics,* 1991.

[158] A. Schwetz, "Boron carbide, boron nitride, and metal borides," *Ullmann's Encyclopedia of Industrial Chemistry,* vol. 6, 1999.

[159] H. Lee and R. Speyer, "Hardness and fracture toughness of pressureless-sintered boron carbide (B4C)," *J. Am. Ceram. Soc,* vol. 85, no. 5, pp. 1291-1293, 2002.

[160] S. Yamada, K. Hirao, Y. Yamauchio and S. Kanzaki, "B4C−CrB2 composites with improved mechanical properties," *Journal of the European Ceramic Society ,* vol. 23, no. 3, pp. 561-565, 2003.

[161] S. Dole, S. Prochazka and R. Doremus, "Microstructural coarsening during sintering of boron Ccrbide," *Journal of the American Ceramic Society ,* vol. 72, no. 6, pp. 958-966, 1989.

[162] N. Orlovskaya, M. Lugovy, V. Subbotin, O. Radchenko, J. Adams, M. Chheda, J. Shih and J. Sankar, "Robust design and manufacturing of ceramic laminates with controlled thermal residual stresses for enhanced toughness," *Journal of Materials Science,* vol. 40, no. 20, pp. 5483-5490, 2005.

[163] N. Orlovskaya, S. Yarmolenko, J. Sankar, J. Kuebler and M. Lugovy, "Effects of rolling and hot pressing on mechanical properties of boron carbide-based ceramics," *Journal of Materials Science,* vol. 43, no. 17, pp. 5942-5947, 2008.

[164] K. Schwetz, W. Grellner and A. Lipp, "Mechanical properties of HIP treated sintered boron carbide," *Inst. Phys.,* vol. 75, pp. 413-426, 1986.

[165] W. Ji, S. Shakir Rehman , W. Wang, H. Wang, Y. Wang, J. Zhang, F. Zhang and Z. Fu, "Sintering boron carbide ceramics without grain growth by plastic deformation as the dominant densification mechanism," *Scientific Reports* , vol. 5, no. 15827, 2015.

[166] A. Sivkov, I. Rakhmatullin, I. Shanekov and Y. Shanekova, "Boron carbide B4C ceramics with enhanced physico-mechanical properties sintered from multimodal powder of plasma dynamic synthesis," *International Journal of Refractory Metals and Hard Materials,* vol. 78, pp. 85-91, 2019.

[167] S. Eqtesadi, A. Motealleh, F. Perera, P. Miranda, A. Pajares, R. Wendelbo, F. Guiberteau and A. Ortiz, "Fabricating geometrically-complex B4C ceramic components by robocasting and pressureless spark plasma sintering," *Scripta Materialia,* vol. 145, pp. 14-18, 2018.

[168] L. Liu, X. Li, X. He, L. Xu, X. Cao, X. Peng, C. Meng, W. Wang, W. Zhu and Y. Wang, "Sintering dense boron carbide without grain growth under high pressure," *Journal of the American Ceramic Society,* vol. 101, pp. 1289-1297, 2018.

[169] T. Saunders, S. Grasso and M. Reece, "Ultrafast-contactless flash sintering using plasma electrodes," *Scientific Reports,* vol. 6, p. 27222, 2016.

[170] J. Swab, J. Tice, A. Wereszczak and R. Kraft, "Fracture toughness of advanced structural ceramics: Applying ASTM C1421," *Journal of the American Ceramic Society,* vol. 98, no. 2, pp. 607-615, 2014.

[171] S. Conzone, W. Blumenthal and J. Vainer, "Fracture toughness of TiB2 and B4C using the single-edge precracked beam, Indentation Strength, Chevron Notched Beam, and Indentation Strength Methods," *Journal of the American Ceramic Society,* vol. 78, no. 8, pp. 2187-2192, 1995.

[172] V. Kulikovsky, V. Vorlicek, P. Bohac, R. Ctvrtlik, M. Stranyanek, A. Dejneka and L. Jastrabik, "Mechanical properties and structure of amorphous and crystalline B4C films," *Diamond and Related Materials,* vol. 18, no. 1, pp. 27-33, 2009.

[173] A. Nisar, M. Mohsin Khan, S. Bajpai and K. Balani, "Processing, microstructure and mechanical properties of HfB2-ZrB2-SiC composites: Effect of B4C and carbon nanotube reinforcements," *International Journal of Refractory Metals & Hard Materials,* vol. 81, pp. 111-118, 2019.

[174] M. Pavese, P. Fino, C. Badini, A. Ortona and G. Marino, "HfB2/SiC as a protective coating for 2D Cf/SiC composites: Effect of high temperature oxidation on mechanical properties," *Surface and Coating Technology,* vol. 202, pp. 2059-2067, 2008.

[175] J. Lawson, C. Bauschlicher and M. Daw, "Ab initio computations of electronic, mechanical, and thermal properties of ZrB2 and HfB2," *Journal of the Americal Ceramic Society* , vol. 94, no. 10, pp. 3494-3499, 2011.

[176] J. Lawson, M. Daw and C. Bauschlicher, "Lattice thermal conductivity of ultra high temperature ceramics ZrB2 and HfB2 from atomistic simulations," *Journal of Applied Physics* , vol. 110, no. 083507, 2011.

[177] W. Hayami, R. Souda, T. Aizawa and T. Tanaka, "Structural analysis of the HfB2(0001) surface by impact-collision ion scattering spectroscopy," *Surface Science,* vol. 415, no. 3, pp. 433-437, 1998.

[178] M. Gasch, D. Ellerby, E. Irby, S. Beckman, M. Gusman and S. Johnson, "Processing, properties and arc jet oxidation of hafnium diboride/silicon carbide ultra high temperature ceramics," *Joural of Material Science* , vol. 39, pp. 5925-5937, 2004.

[179] S. Chakraborty, A. Mallick, D. Debnath and P. Das, "Densification, mechanical and tribological properties of ZrB2 by SPS: Effect of pulsed current," *Int. Journal of Refractory Metals and Hard Materials,* vol. 48, pp. 150-156, 2015.

[180] E. Zapata-Solvas, D. Jayaseelan, H. Lin, P. Brown and W. Lee, "Mechanical properties of ZrB2- and HfB2-based ultra-high temperature ceramics fabricated by spark plasma sintering," *Journal of the European Ceramic Society,* vol. 33, pp. 1373-1386, 2013.

[181] F. Monteverde, A. Bellosi and L. Scatteia, "Processing and properties of ultra-high temperature ceramics for space applications," *Materials Science and Engineering A,* vol. 485, pp. 415-421, 2008.

[182] S. Song, Z. Wang and G. Shi, "Heating mechanism of spark plasma sintering," *Ceramics International,* vol. 39, pp. 1393-1396, 2013.

[183] R. Chaim, "Electric field effects during spark plasma sintering of ceramic," *Journal of Meterial Science ,* vol. 48, pp. 502-510, 2013.

[184] S.-X. Song, Z. Wang and G.-P. Shi, "Electric field effects during spark plasma sintering of ceramic," *Ceramics International,* vol. 39, pp. 1393-1396, 2013.

[185] C. Musa, R. Orru, D. Sciti, L. Silvestroni and G. Cao, "Synthesis, consolidation and characterization of monolithic and SiC whiskers reinforced HfB2 ceramics," *Journal of the European Ceramic Society,* vol. 33, pp. 603-614, 2013.

[186] S. Zhang, G. Hilmas and W. Fahrenholtz, "Mechanical properties of sintered ZrB2–SiC ceramics," *Journal of the European Ceramic Society,* vol. 31, pp. 893-901, 2011.

[187] G. Pathalinga Prasad , H. Chittappa, M. Nagaral and V. Auradi, "Influence of 40 micron size B4C particulates addition on mechanical behavior of LM29 alloy composites," *Journal of Engineering,* vol. 8, no. 2, pp. 20-27, 2018.

[188] A. Suri, C. Subramanian, J. Sinber and T. Murthy, "Synthesis and consolidation of boron carbide: a review," *Full Terms & Conditions of access and use can be found at https://www.tandfonline.com/action/journalInformation?journalCode=yimr20 International Materials Reviews,* vol. 55, no. 1, pp. 4-40, 2010.

[189] B. Niu, F. Zhang, J. Zhang, W. Ji, W. Wang and Z. Fu, "Ultra-fast densification of boron carbide by flash spark plasma sintering," *Scripta Materialia,* vol. 116, pp. 127-130, 2016.

[190] V. Mamedov, "Spark plasma sintering as advanced PM sintering method," *Powder Metallurgy,* vol. 45, no. 4, pp. 322-328, 2013.

[191] J. Zou, S. Grasso, L. Liu, H. Ma, M. Reece and J. Binner, "Flash spark plasma sintering of HfB2 ceramics without pre-sintering," *Scripta Materialia,* vol. 156, pp. 115-119, 2018.

[192] J. Lawson, C. Bauschlicher and M. Daw, "Ab initio computations of electronic, mechanical, and thermal properties of ZrB2 and HfB2," *J. Am. Ceram. Soc.,,* vol. 94, no. 10, pp. 3494-3499, 2011.

[193] G. Duvaut, "Analyse fonctionnelle et mécanique des milieux continus–Application à l'étude des matériaux composites à structure périodique–homogénéisation," in *Theoretical and applied mechanics*, Amsterdam, North Holland Publishing , 1976.

[194] F. Devries, H. Dumontet, G. Duvaut and F. Lene, "Homogenization and damage for composite structures," *lnternat. J. Numer. Methods Engrg*, vol. 27, pp. 285-298, 1989.

[195] "A material based finite element analysis of heterogeneous media involving Dirichlet tessellations," *Computer Methods in Applied Mechanics and Engineering*, vol. 104, pp. 211-247, 1992.

[196] H. Suemasu, A. Kondo, K. Itatani and A. Nozue, "A probabilistic approach to the toughening mechanism in short-fiber-reinforced ceramic-matrix composites," *Composites Science and Technology*, vol. 61, no. 2, pp. 281-288, 2001.

[197] T. Csanadi, A. Kovalcikova, J. Dusza, W. Fahrenholtz and G. Hilmas, "Slip activation controlled nanohardness anisotropy of ZrB2 ceramic grains," *Acta Materialia*, vol. 140, pp. 452-464, 2017.